Digest Journal of Nanomaterials and Biostructures

Dig. J. Nanomater. Bios. **2026**; 21(2): 53673
https://doi.org/10.31083/DJNB53673

Original Research

Gamma Irradiation-Engineered g-C_3N_4 Nanosheets via Electrochemical Exfoliation for Enhanced Photocatalytic Degradation of Methylene Blue

Ahmed Mostafa[1,*], Mahmoud A. Ibrahim[1], Hesham A. Yousef[1], Adel Ashour[2]

[1]Physics Department, Faculty of Science, Suez University, 43511 Suez, Egypt
[2]Physics Department, Faculty of Science, Islamic University of Madinah, 42351 Madinah, Saudi Arabia
*Correspondence: amostafa0004@gmail.com (Ahmed Mostafa)

Academic Editor: Carmen-Georgeta Ristoscu
Submitted: 20 November 2025 Revised: 28 January 2026 Accepted: 6 February 2026 Published: 8 May 2026

Abstract

Graphitic carbon nitride (g-C_3N_4) has attracted sustained interest as a visible-light-driven photocatalyst; however, its practical efficiency is often constrained by limited surface accessibility and rapid recombination of photogenerated charge carriers. Herein, g-C_3N_4 nanosheets were prepared via an environmentally benign electrochemical exfoliation route and subsequently modified through controlled gamma irradiation (γ-irradiation) in the dose range of 0–50 kGy. Structural analysis revealed that the crystalline framework of g-C_3N_4 remained preserved after irradiation, while the average crystallite size decreased from ~24.6 to ~18.4 nm, accompanied by an increase in lattice microstrain from 2.05×10^{-3} to 2.68×10^{-3}. Optical characterization demonstrated dose-dependent tuning of the band structure, with direct band gap energies shifting from ~3.0 to ~3.2 eV and indirect transition energies ranging from ~2.4 to ~2.7 eV. Photoluminescence (PL) and time-resolved measurements indicated a pronounced suppression of non-radiative recombination at moderate irradiation levels, with the carrier lifetime reaching a maximum of ~4.6 ns at ~25 kGy. In parallel, γ-irradiation induced a measurable enhancement in surface area and pore characteristics. These combined effects resulted in a marked improvement in visible-light photocatalytic degradation of methylene blue (MB), following pseudo-first-order kinetics. The results demonstrate that γ-irradiation provides an effective and contamination-free means of optimizing the structural and photophysical properties of g-C_3N_4 nanosheets for photocatalytic applications.

Keywords: g-C_3N_4 nanosheets; γ-irradiation; electrochemical exfoliation; photocatalysis; methylene blue degradation; charge-carrier dynamics

1. Introduction

Graphitic carbon nitride (g-C_3N_4) has emerged as a promising metal-free photocatalyst owing to its suitable band gap, chemical stability, and facile synthesis from earth-abundant precursors. Its ability to absorb visible light renders it particularly attractive for photocatalytic environmental remediation. Nevertheless, bulk g-C_3N_4 commonly exhibits strong interlayer stacking, low specific surface area, and inefficient charge-carrier separation, all of which substantially limit its photocatalytic performance [1–4].

Considerable efforts have therefore been devoted to overcoming these intrinsic limitations through structural modification strategies such as nano-structuring, defect engineering, and exfoliation into two-dimensional architectures [5–7]. Among these approaches, exfoliation into nanosheets is especially effective in enhancing surface exposure and shortening charge-transport pathways. However, exfoliation alone often offers limited control over defect type and density, parameters that critically govern electronic structure and charge-carrier dynamics [8–10].

High-energy gamma irradiation (γ-irradiation) has recently been recognized as a versatile post-synthetic tool capable of inducing controlled lattice distortions and defect states without introducing chemical impurities. Through precise dose regulation, γ-irradiation enables fine modulation of optical and electronic properties, potentially improving light absorption and suppressing charge recombination [11–13]. Despite this potential, systematic investigations combining electrochemical exfoliation with γ-irradiation for g-C_3N_4 nanosheets remain limited, particularly with respect to establishing clear correlations between irradiation dose, microstructural evolution, and photocatalytic activity [14,15].

Accordingly, the objective of the present work is to address this gap by developing γ-irradiation-engineered g-C_3N_4 nanosheets via a green electrochemical exfoliation approach and to elucidate, in a systematic manner, the dose-dependent effects of γ-irradiation on their structural, optical, textural, and photocatalytic properties. By integrating comprehensive characterization with photocatalytic performance evaluation, this study aims to provide deeper insight into structure–property–activity relationships in irradiated g-C_3N_4 systems.

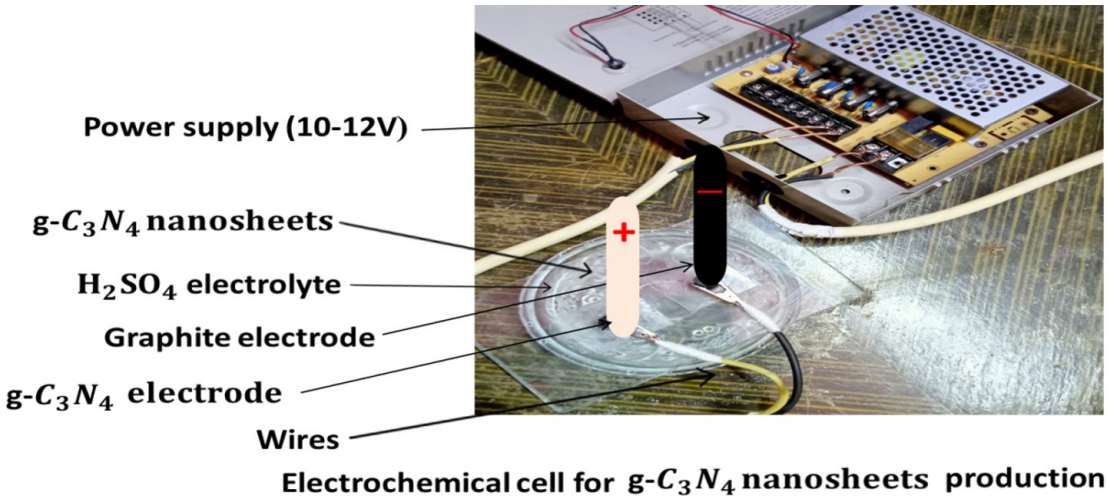

Fig. 1. Schematic illustration of the synthesis of g-C_3N_4 nanosheets from Urea using a novel method. g-C_3N_4, Graphitic carbon nitride.

2. Materials and Methods

2.1 Materials

All experiments were performed using a standard electrochemical cell coupled with a regulated direct current (DC) power supply (PHYWE DC Power Supply 0–12 V/5 A, PHYWE Systeme GmbH & Co. KG, Göttingen, Germany). Sulfuric acid (H_2SO_4, 95%–98%, Merck, Cat. No. 100731 Darmstadt, Germany) was employed as the electrolyte at various concentrations. Graphite electrodes prepared from recycled carbon sources (spent batteries) and g-C_3N_4 electrodes synthesized from analytical-grade urea ($CO(NH_2)_2$, ≥99%: Sigma-Aldrich, Cat. No. U5128, St. Louis, MO, USA) were used as the working electrodes.

2.1.1 Novel Green Synthesis of g-C_3N_4 Nanosheets

g-C_3N_4 was synthesized using analytical-grade urea ($CO(NH_2)_2$, ≥99% purity) as the precursor. In a typical synthesis, 10 g of urea was placed in a covered alumina crucible and thermally treated in a programmable muffle furnace (Nabertherm LHT 04/17, Nabertherm GmbH, Lilienthal, Lower Saxony, Germany) at temperatures ranging from 400 °C to 650 °C for 3 h in ambient air, employing a heating rate of 5 °C min^{-1}. During the thermal polymerization process, urea decomposed into gaseous by-products such as NH_3 and CO_2, resulting in the formation of a yellow solid corresponding to bulk g-C_3N_4, as illustrated in Fig. 1. The obtained material was collected, finely ground, and stored in airtight containers for subsequent use. Exfoliated g-C_3N_4 nanosheets were prepared via a simple and efficient electrochemical exfoliation approach. The electrochemical cell comprised two electrodes: a graphite electrode fabricated from recycled carbon sources (e.g., spent batteries) and a g-C_3N_4 electrode synthesized from urea. An acidic electrolyte, typically H_2SO_4 at various concentrations, was employed, and a DC power supply delivering 10–12 V was applied to promote interlayer expansion and exfoliation of g-C_3N_4, as shown in Fig. 1. Upon completion of the exfoliation process, the resulting suspension was allowed to stand until complete sedimentation of the solid product. The precipitate was then collected, repeatedly washed with deionized water, and dried in a laboratory oven (Memmert UN55, Memmert GmbH, Schwabach, Bavaria, Germany) at 50–60 °C to obtain fine g-C_3N_4 nanosheet powder. To evaluate the influence of post-thermal treatment, the exfoliated nanosheets were subsequently annealed at temperatures between 400 °C and 650 °C under controlled conditions [16–18]. This annealing process enabled a systematic investigation of the effects of heat treatment on the crystallinity, stacking order, and physicochemical properties of the g-C_3N_4 nanosheets, as discussed in the Results and Discussion section.

2.1.2 γ-Irradiation Treatment of g-C_3N_4 Nanosheets

The g-C_3N_4 nanosheets were subjected to γ-irradiation using a ^{60}Co source at the National Center for Radiation Research and Technology (NCRRT), Cairo, Egypt [19,20]. Irradiation was performed at room temperature under ambient atmospheric conditions, with absorbed doses ranging from 5 to 50 kGy. The dose rate was accurately calibrated prior to each irradiation run to ensure uniform energy delivery to the samples. During exposure, the nanosheets were sealed in quartz vials to prevent contamination and to preserve their structural integrity. This controlled γ-irradiation process was designed to induce defect states, modify surface characteristics, and promote structural rearrangements within the g-C_3N_4 framework. Systematic variation of the irradiation dose enabled a reliable evaluation of dose-dependent changes in crystallinity, electronic structure, optical properties, and photocatalytic performance, as discussed in the Results and Discussion section.

2.2 Characterization Tools

2.2.1 XRD Technique

X-ray diffraction (XRD) measurements were employed to investigate the crystallographic structure and irradiation-induced microstructural changes in bulk g-C_3N_4 and exfoliated g-C_3N_4 nanosheets. The diffraction patterns were recorded using (D8 Advance, Bruker AXS GmbH, Karlsruhe, Germany, Cu Kα radiation, λ = 1.5406 Å) over a 2θ range of 5°–90°. Structural parameters were quantitatively evaluated using the most intense (002) reflection located at approximately $2\theta \approx 27.4°$, which is associated with the interlayer stacking of the conjugated g-C_3N_4 framework. The crystallite size (D) was estimated using the Scherrer Eqn. 1 [21,22]:

$$D = \frac{0.9\lambda}{\beta \cos\theta} \quad (1)$$

where λ is the wavelength, β is the full width at half maximum (FWHM) of the (002) peak expressed in radians, and θ is the Bragg angle. The lattice microstrain (ε) was calculated following the Williamson–Hall approximation [6,22]:

$$\varepsilon = \frac{\beta}{4 \tan\theta} \quad (2)$$

The dislocation density (δ), which reflects the defect concentration within the crystalline domains, was determined using the relation [22,23]:

$$\delta = \frac{1}{D^2} \quad (3)$$

The derived parameters should be regarded as approximate values, as instrumental broadening effects were not explicitly subtracted. This approach is widely adopted for comparative studies aimed at elucidating relative structural changes induced by external treatments such as γ-irradiation. In addition, the XRD data were subjected to Rietveld refinement to extract detailed microstructural parameters using the MAUD software package (version 2.94, developed by University of Trento, Trento, Italy). Complementary peak analysis and phase identification were performed with X'Pert HighScore Plus software (version 4.9, Malvern Panalytical B.V., Almelo, The Netherlands) where required [9,10].

2.2.2 Microscopic Characterization of Bulk g-C_3N_4 and Nanosheets

The morphology and size of the synthesized nanostructures were examined using a high-resolution scanning electron microscope (SEM, JEOL JSM-IT200, Tokyo, Japan) operated at an accelerating voltage of 25 kV. The structural features and dimensional characteristics of bulk g-C_3N_4 and its exfoliated nanosheets were further investigated by high-resolution transmission electron microscopy (HRTEM, JEOL 3010, JEOL Ltd., Tokyo, Japan) operated at 200 kV [11]. Additional morphological analysis and uniformity assessment were performed using a ZEISS EVO-MA10 scanning electron microscope equipped with an energy-dispersive X-ray spectroscopy (EDX) detector (Carl Zeiss Microscopy GmbH, Oberkochen, Baden-Württemberg, Germany), enabling simultaneous evaluation of surface morphology and elemental composition. SEM images were processed using ImageJ software (version 1.53, National Institutes of Health, Bethesda, MD, USA) to determine particle size distributions based on statistical analysis of more than 100 particles per sample. Elemental composition obtained from EDX measurements was analyzed using the instrument-integrated AZtecEnergy EDX analysis software (version 3.3, Oxford Instruments NanoAnalysis Ltd., High Wycombe, Buckinghamshire, UK) [11,12].

2.2.3 Raman Spectroscopy Test

Raman spectra were recorded using an inVia Raman spectrometer (Renishaw plc, Gloucestershire, UK) equipped with a thermoelectrically cooled charge-coupled device (CCD) detector maintained at –80 °C. A He–Ne laser with an excitation wavelength of 532 nm was employed, with the laser power restricted to 1 mW to prevent sample heating. The integration time for each measurement was set to 100 s.

2.2.4 UV–Vis Diffuse Reflectance Spectroscopy

The optical absorption properties of the prepared g-C_3N_4 nanosheets were examined by ultraviolet–visible diffuse reflectance spectroscopy (UV–Vis DRS) using a Shimadzu UV-2600 UV–Vis spectrophotometer (Shimadzu Corporation, Kyoto, Japan) equipped with an integrating sphere accessory (ISR-2600Plus). The measurements were carried out at room temperature over the wavelength range of 200–800 nm. Barium sulfate ($BaSO_4$) was employed as a non-absorbing reflectance standard, and all spectra were collected under identical conditions to ensure reliable comparison among samples subjected to different γ-irradiation doses. The obtained diffuse reflectance data were converted to the corresponding absorption spectra using the Kubelka–Munk function (Eqn. 4) [12,13]:

$$F(R) = \frac{(1-R)^2}{2R} \quad (4)$$

where R is the measured reflectance. The optical band gap energies were estimated by constructing Tauc plots based on the Kubelka–Munk-transformed data, assuming both direct and indirect electronic transitions for g-C_3N_4. Linear extrapolation of the absorption edge to the energy axis was used to determine the band gap values. All DRS measure-

ments were repeated to confirm reproducibility. This characterization provides essential information on irradiation-induced changes in light absorption behavior and electronic structure of the g-C_3N_4 nanosheets.

2.2.5 BET Surface Area and Porosity Analysis

The specific surface area and pore structure of the prepared g-C_3N_4 nanosheets were evaluated by nitrogen adsorption–desorption measurements using a Micromeritics ASAP 2020 surface area and porosity analyzer (Micromeritics Instrument Corporation, Norcross, GA, USA). Prior to analysis, all samples were degassed under vacuum at 150 °C for 12 h to remove physically adsorbed moisture and residual gases [12–14]. Nitrogen adsorption–desorption isotherms were recorded at 77 K over a relative pressure (P/P_0) range of 0.01–0.99. The specific surface area was calculated using the Brunauer–Emmett–Teller (BET) method within the relative pressure range of 0.05–0.30, where a linear BET plot was obtained. The total pore volume was estimated from the amount of nitrogen adsorbed at a relative pressure close to unity ($P/P_0 \approx 0.99$). Pore size distribution curves were derived from the adsorption branch of the isotherms using the Barrett–Joyner–Halenda (BJH) method, assuming cylindrical pore geometry [11,13,15]. All measurements were conducted under identical experimental conditions to ensure meaningful comparison among samples subjected to different γ-irradiation doses. The BET analysis provides insight into irradiation-induced changes in surface area, pore volume, and pore size distribution, which are key parameters influencing adsorption capacity and photocatalytic performance.

2.2.6 Photoluminescence Characterization

Photoluminescence (PL) spectroscopy was employed to investigate the electronic structure, defect-related states, and charge-carrier recombination behavior of the prepared g-C_3N_4 nanosheets before and after γ-irradiation. Steady-state PL measurements were carried out at room temperature using an Edinburgh Instruments FLS1000 fluorescence spectrometer (Edinburgh Instruments Ltd., Livingston, Scotland, UK) equipped with a continuous-wave xenon lamp as the excitation source. The excitation wavelength was fixed at 350 nm, corresponding to the intrinsic absorption of g-C_3N_4, while the emission spectra were recorded over the wavelength range of 380–650 nm [12,16]. All spectra were collected under identical experimental conditions to ensure reliable comparison among samples subjected to different γ-irradiation doses. Time-resolved photoluminescence (TRPL) measurements were performed using the same system operated in time-correlated single-photon counting (TCSPC) mode. A pulsed diode laser with an excitation wavelength of 375 nm was employed, and the emission decay profiles were monitored at the dominant PL emission wavelength of each sample. The obtained decay curves were fitted using a multi-exponential decay model to extract the average lifetime and individual decay components, which provide insight into the relative contributions of radiative recombination and defect-assisted non-radiative processes [17,18]. All PL and TRPL measurements were repeated to confirm reproducibility. The extracted lifetimes and emission intensities were analyzed comparatively to evaluate the influence of γ-irradiation dose on charge-carrier recombination dynamics. This PL characterization approach enables a reliable assessment of irradiation-induced defect states and their role in modulating the photophysical properties of g-C_3N_4 nanosheets.

2.2.7 Photocatalytic Degradation Analysis

The photocatalytic activity of the synthesized g-C_3N_4 nanosheets was evaluated through the degradation of methylene blue (MB) under visible-light irradiation. A 300 W xenon lamp equipped with a cutoff filter (λ >420 nm) was employed as the light source to simulate visible solar irradiation. In a typical photocatalytic experiment, 50 mg of the photocatalyst was dispersed in 100 mL of an aqueous MB solution with an initial concentration of 10 mg L^{-1} under continuous magnetic stirring to ensure homogeneous suspension.

Prior to light exposure, the reaction mixture was stirred in the dark for 30 min to establish adsorption–desorption equilibrium between MB molecules and the catalyst surface. Upon visible-light irradiation, aliquots of 3 mL were withdrawn at regular intervals of 20 min, centrifuged to remove suspended catalyst particles, and subsequently analyzed using a UV–Vis spectrophotometer. The residual concentration of MB was determined by monitoring the characteristic absorption maximum at 664 nm [19–21]. The photocatalytic degradation efficiency (D%) was calculated using the following Eqn. 5:

$$D\% = \frac{C_0 - C_t}{C_0} \times 100 \tag{5}$$

where C_0 and C_t represent the MB concentrations at the initial time and at irradiation time t, respectively. The degradation kinetics were analyzed using a pseudo-first-order kinetic model, expressed as Eqn. 6 [16]:

$$\ln\left(\frac{C_0}{C_t}\right) = kt \tag{6}$$

where k (min^{-1}) denotes the apparent first-order rate constant. This kinetic approach enables a quantitative comparison of the photocatalytic performances of g-C_3N_4 samples prepared under different synthesis temperatures and γ-irradiation doses, while providing a consistent framework for evaluating their relative activity, stability, and reusability under visible-light irradiation.

To gain insight into the reactive species involved in the photocatalytic degradation process, scavenger experiments were conducted under otherwise identical experimental conditions. Isopropyl alcohol (IPA, 10 mM, ≥99.5%, Cat. No. 278475, Sigma-Aldrich, St. Louis, MO, USA), p-benzoquinone (BQ, 1 mM, ≥98%, Cat. No. B10358, Sigma-Aldrich, St. Louis, MO, USA), and ethylenediaminetetraacetic acid (EDTA, 2 mM, ≥99%, Cat. No. E5134, Sigma-Aldrich, St. Louis, MO, USA) were employed as selective quenchers for hydroxyl radicals (•OH), superoxide radicals ($\bullet O_2^-$), and photogenerated holes (h^+), respectively. The scavengers were added to the reaction system after the adsorption–desorption equilibrium was reached and before visible-light irradiation. The resulting changes in photocatalytic degradation efficiency were analyzed to elucidate the relative contributions of the different reactive species to the MB degradation process [13,16,17].

3. Results

3.1 XRD Analysis of Bulk and Exfoliated g-C_3N_4 Under γ-Irradiation

Fig. 2a and Fig. 2b present the XRD patterns of bulk g-C_3N_4 and exfoliated g-C_3N_4 nanosheets synthesized at 550 °C and subjected to γ-irradiation doses ranging from 0 to 50 kGy. In both materials, the characteristic diffraction peaks located at approximately 13.1° and 27.4° are retained, corresponding to the (100) in-plane structural periodicity of tri-s-triazine units and the (002) interlayer stacking of the conjugated aromatic framework, respectively. Quantitative evaluation of the diffraction data was performed using the (002) reflection to estimate the crystallite size, lattice microstrain, and dislocation density according to Eqns. 1,2,3, with the calculated values summarized in Table 1 for bulk g-C_3N_4 and Table 2 for exfoliated g-C_3N_4 nanosheets.

As shown in Table 1, the apparent crystallite size of bulk g-C_3N_4 decreases gradually with increasing irradiation dose, while the corresponding microstrain and dislocation density increase systematically. This trend indicates progressive accumulation of irradiation-induced lattice distortions and defect sites, without evidence of phase transformation or long-range structural disruption, as further supported by the absence of peak shifts or secondary diffraction features in Fig. 2a. In the case of exfoliated g-C_3N_4 nanosheets (Fig. 2b and Table 2), the calculated crystallite sizes are consistently smaller and the microstrain values higher than those of the bulk material at all irradiation doses, reflecting reduced interlayer coherence associated with the exfoliation process.

With increasing γ-irradiation dose, both microstrain and dislocation density show a further incremental increase, while the characteristic g-C_3N_4 diffraction peaks remain preserved, confirming that the fundamental crystalline framework is maintained up to 50 kGy [3,15,22]. Overall, the trends observed in Tables 1,2 are in good agreement with the peak-broadening behavior evident in Fig. 2a,b. The

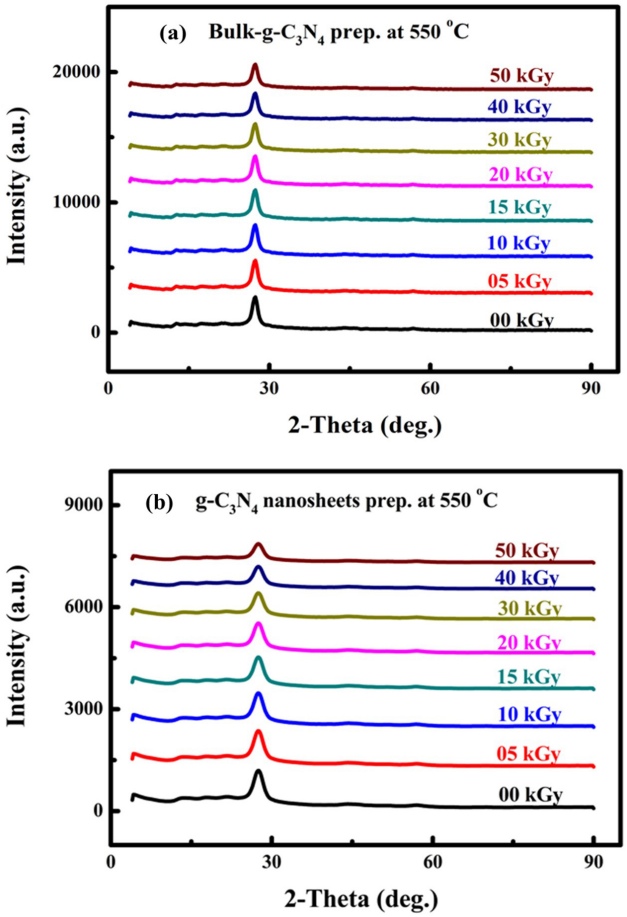

Fig. 2. XRD patterns of g-C_3N_4 materials under γ-irradiation. (a) XRD patterns of bulk g-C_3N_4 prepared at 550 °C under different γ-irradiation doses. (b) XRD patterns of g-C_3N_4 nanosheet prepared at 550 °C under different γ-irradiation doses. XRD, X-ray diffraction. γ-irradiation, gamma irradiation.

combined analysis based on Eqns. 1,2,3 demonstrates that γ-irradiation primarily affects microstructural parameters such as crystallite size, lattice strain, and defect density, while preserving the long-range crystallographic structure of both bulk and exfoliated g-C_3N_4.

3.2 Vibrational Features of g-C_3N_4 Nanosheets Under γ-Irradiation

Fig. 3 illustrates the Fourier-transform infrared spectroscopy (FTIR) spectra of exfoliated g-C_3N_4 nanosheets synthesized at 550 °C and subjected to γ-irradiation doses ranging from 0 to 50 kGy. All spectra exhibit the characteristic vibrational features of graphitic carbon nitride, confirming that the fundamental chemical framework of the material is preserved following irradiation.

The broad absorption band observed in the region of 3000–3400 cm^{-1} is attributed to stretching vibrations of N–H and O–H groups, which may originate from terminal amine functionalities and adsorbed moisture on the nanosheet surface [23,24]. The group of intense bands lo-

Table 1. Crystallite size, microstrain, and dislocation density of bulk g-C_3N_4 derived from XRD analysis at different γ-irradiation doses.

Dose (kGy)	D (nm)	ε ($\times 10^{-3}$)	δ ($\times 10^{15}$ m^{-2})
0	~39.8	1.21	0.63
10	~36.5	1.33	0.75
20	~33.9	1.46	0.87
30	~31.6	1.58	1.00
40	~30.2	1.65	1.10
50	~28.9	1.72	1.20

Table 2. Crystallite size, microstrain, and dislocation density of exfoliated g-C_3N_4 derived from XRD analysis at different γ-irradiation doses.

Dose (kGy)	D (nm)	ε ($\times 10^{-3}$)	δ ($\times 10^{15}$ m^{-2})
0	~24.6	2.05	1.65
10	~22.9	2.18	1.91
20	~21.4	2.31	2.18
30	~20.1	2.45	2.47
40	~19.2	2.57	2.71
50	~18.4	2.68	2.95

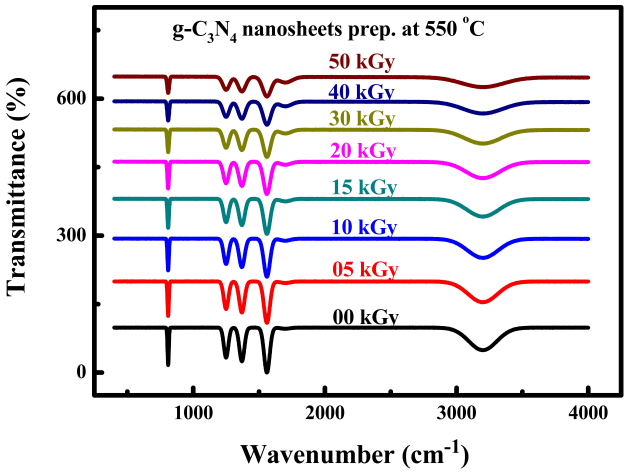

Fig. 3. FTIR spectra of g-C_3N_4 nanosheets prepared at 550 °C under different γ-irradiation doses. FTIR, Fourier-transform infrared spectroscopy.

cated between approximately 1200 and 1650 cm^{-1} corresponds to the stretching modes of C–N and C=N bonds within the heterocyclic tri-s-triazine units, which constitute the backbone of the g-C_3N_4 structure. In addition, the distinct band centered near 810 cm^{-1} is assigned to the breathing mode of the tri-s-triazine ring, serving as a fingerprint vibration of polymeric g-C_3N_4. With increasing γ-irradiation dose, no new absorption bands are detected, and no disappearance of existing peaks is observed, indicating the absence of chemical decomposition or phase transformation. However, subtle variations in band intensity and slight broadening of selected vibrational modes can be discerned at higher doses, suggesting localized structural disorder or modification of surface functional groups induced by irradiation. These changes are consistent with irradiation-induced defect formation and bond distortion rather than alterations to the primary chemical structure. Overall, the FTIR results demonstrate that γ-irradiation up to 50 kGy does not disrupt the intrinsic molecular architecture of exfoliated g-C_3N_4 nanosheets, while inducing minor modifications in local bonding environments.

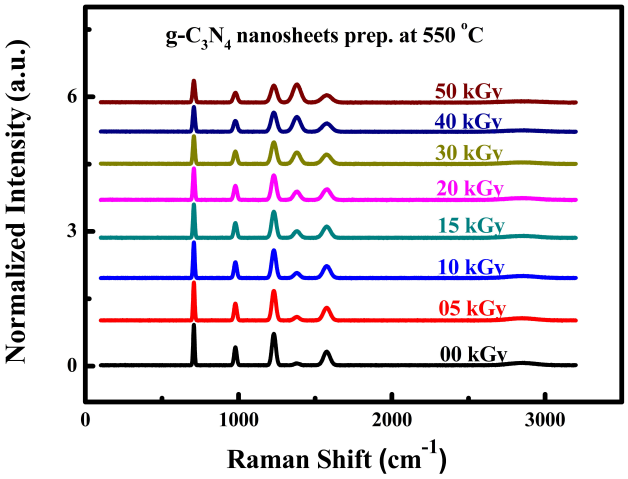

Fig. 4. Raman spectra of g-C_3N_4 nanosheets prepared at 550 °C under different γ-irradiation doses.

3.3 Effect of γ-Irradiation on the Raman Spectra of g-C_3N_4 Nanosheets

Fig. 4 illustrates the Raman spectra of g-C_3N_4 nanosheets synthesized at 550 °C and subjected to γ-irradiation doses ranging from 0 to 50 kGy. All spectra exhibit the characteristic vibrational features of graphitic carbon nitride, confirming that the fundamental molecular framework is preserved irrespective of irradiation dose. The prominent bands observed in the region between ~700 and 1700 cm^{-1} are attributed to the breathing modes of tri-s-triazine units and the stretching vibrations of conjugated C–N heterocycles, which are hallmarks of the g-C_3N_4 structure. Notably, the overall spectral profiles remain largely unchanged with increasing irradiation dose, indicating that gamma exposure does not induce significant chemical transformation or phase alteration within the detection limits of Raman spectroscopy [19,20]. However, a gradual variation in band intensity and slight peak broadening can be discerned at higher doses, particularly above 30 kGy. These changes may be indicative of irradiation-induced lattice disorder, localized bond distortion, or an increased defect population within the polymeric network. Such effects are consistent with microstructural perturbations rather than long-range structural reorganization. Importantly, no new Raman bands or peak shifts associated

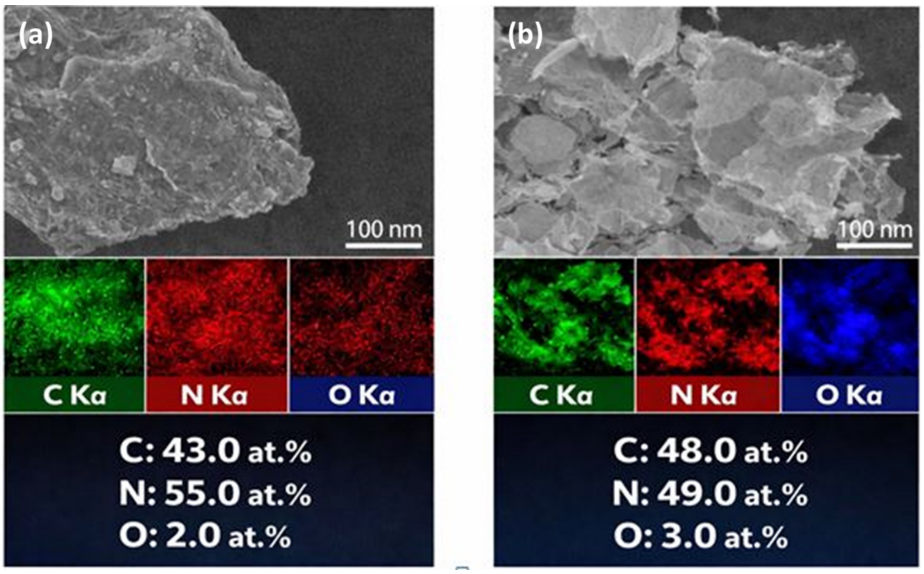

Fig. 5. SEM images and EDX elemental mapping of (a) bulk g-C_3N_4 and (b) exfoliated g-C_3N_4 nanosheets, showing the distribution of C (Kα), N (Kα), and O (Kα) and their corresponding atomic percentages. Both samples exhibit uniform bulk elemental distribution and preserved stoichiometry, with no detectable impurities after exfoliation. SEM, scanning electron microscope; EDX, energy-dispersive X-ray spectroscopy. Scale bar = 100 nm.

with secondary phases or bond cleavage are detected, underscoring the structural robustness of g-C_3N_4 nanosheets under γ-irradiation up to 50 kGy. It should be emphasized that Raman spectroscopy primarily provides qualitative insight into vibrational and bonding environments; therefore, the observed spectral variations are interpreted as indicative trends rather than definitive evidence of defect formation. Overall, the Raman results support the conclusion that γ-irradiation predominantly introduces subtle microstructural modifications while preserving the intrinsic framework of g-C_3N_4 nanosheets [25].

3.4 Elemental Composition Analysis of Bulk and Exfoliated g-C_3N_4

EDX elemental mapping was employed to examine the bulk compositional uniformity of g-C_3N_4 before and after exfoliation, as shown in Fig. 5a,b. It should be noted that EDX provides semi-quantitative elemental information from a near-surface bulk region and is therefore used here to assess overall elemental distribution rather than surface-specific chemistry. The EDX maps of bulk g-C_3N_4 (Fig. 5a) reveal a homogeneous and continuous distribution of carbon and nitrogen across the analyzed area, with no evidence of elemental segregation. Quantitative analysis indicates atomic percentages of approximately 43.0 at.% C, 55.0 at.% N, and 2.0 at.% O, consistent with the expected stoichiometry of polymeric g-C_3N_4 and indicative of a chemically stable framework. In comparison, the exfoliated g-C_3N_4 nanosheets (Fig. 5b) exhibit spatially overlapping C and N signals localized within thinner, flake-like regions, reflecting the nanosheet morphology produced by the exfoliation process [6,9].

The corresponding elemental composition comprises 48.0 at.% C, 49.0 at.% N, and a slightly increased oxygen content of 3.0 at.%. The modest increase in oxygen is plausibly attributed to surface-exposed edge sites or mild oxidation during exfoliation, rather than the incorporation of extraneous phases. Importantly, no additional elemental signals are detected in either sample, confirming the high purity of the materials.

Overall, the comparative EDX results demonstrate that exfoliation preserves the intrinsic C–N framework and bulk stoichiometry of g-C_3N_4, while inducing morphological thinning without compromising compositional integrity—an essential prerequisite for maintaining reliable physicochemical and photocatalytic performance.

3.5 SEM Micrographs of Bulk g-C_3N_4 and Exfoliated g-C_3N_4 Nanosheets

The morphological characteristics of bulk and exfoliated g-C_3N_4 were examined by field-emission scanning electron microscopy (FESEM), as shown in Fig. 6a,c present FESEM images of bulk g-C_3N_4 recorded at low and high magnifications, respectively, revealing densely packed, irregular agglomerates composed of thick, stacked plate-like structures with lateral dimensions predominantly in the sub-micron range. This compact morphology indicates strong interlayer interactions and limited exposure of accessible surface sites. In contrast, Fig. 6b,d display FESEM images of exfoliated g-C_3N_4 nanosheets at corresponding magnifications. As observed in Fig. 6b, the bulk agglomerates are transformed into loosely stacked, sheet-like assemblies with reduced lateral dimensions, while the higher-magnification image in Fig. 6d clearly reveals thin-

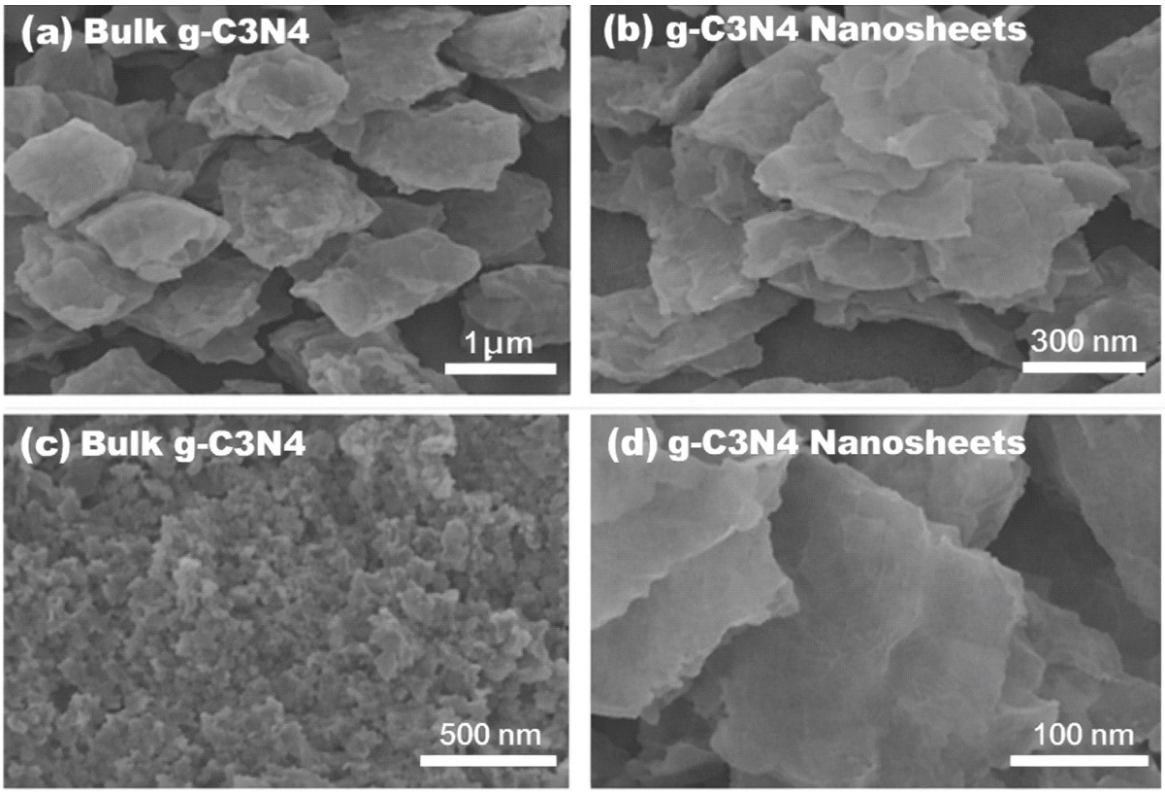

Fig. 6. FESEM images of g-C_3N_4 showing (a,c) bulk material with stacked, dense morphology and (b,d) exfoliated nanosheets with thin, layered structures at low and high magnifications. FESEM, field-emission scanning electron microscopy. Fig. 6a scale bar = 1 µm; Fig. 6b scale bar = 300 nm; Fig. 6c scale bar = 500 nm; Fig. 6d scale bar = 100 nm.

ner, delaminated layers with smoother surfaces. Although the lateral sizes of the exfoliated sheets remain within the sub-micron regime, the evident delamination and structural thinning relative to the bulk material confirm the effectiveness of the exfoliation process. Such morphological evolution is expected to enhance surface accessibility and improve interfacial contact with reactant molecules, which is advantageous for photocatalytic applications, without invoking strict size-based classification as nanomaterials [26].

3.6 Structural Evolution of Bulk g-C_3N_4 Into Exfoliated Nanosheets

Fig. 7 presents transmission electron microscopy (TEM) images illustrating the morphological differences between bulk g-C_3N_4 and exfoliated g-C_3N_4 nanosheets at various magnifications. In Fig. 7a, the bulk g-C_3N_4 appears as a compact, nearly spherical agglomerate composed of densely packed layers, indicating strong interlayer interactions and significant material thickness. Fig. 7c further reveals the internal texture of the bulk sample, where the dark contrast and limited transparency confirm the presence of thick, highly stacked domains with restricted accessibility of surface sites. In contrast, Fig. 7b shows the exfoliated g-C_3N_4 in the form of extended, sheet-like structures with markedly enhanced transparency, reflecting a pronounced reduction in thickness. The layered and partially overlapping nature of the nanosheets is clearly visible, demonstrating successful delamination of the bulk precursor. This observation is further supported by Fig. 7d, which highlights ultrathin, flexible nanosheets with smooth surfaces and folded edges, characteristic of two-dimensional architectures. Collectively, the TEM images in Fig. 7 confirm the effective transformation of bulk g-C_3N_4 into ultrathin nanosheets, accompanied by increased structural openness and surface exposure, which are advantageous for charge transport and surface-dominated processes [27].

3.7 Optical Properties and Band Gap Analysis of γ-Irradiated g-C_3N_4 Nanosheets

The optical properties of g-C_3N_4 nanosheets synthesized at 550 °C and exposed to γ-irradiation doses ranging from 0 to 50 kGy were systematically investigated using UV–Vis DRS, absorption analysis, Kubelka–Munk transformation, and Tauc plot evaluation. The combined results demonstrate that γ-irradiation induces subtle yet measurable modifications in the optical band structure of g-C_3N_4 while preserving its intrinsic semiconducting framework [28]. Diffuse reflectance and absorption spectra reveal slight shifts in the absorption edge with increasing irradiation dose, suggesting defect-assisted modulation of electronic transitions. Further analysis using the Kubelka–

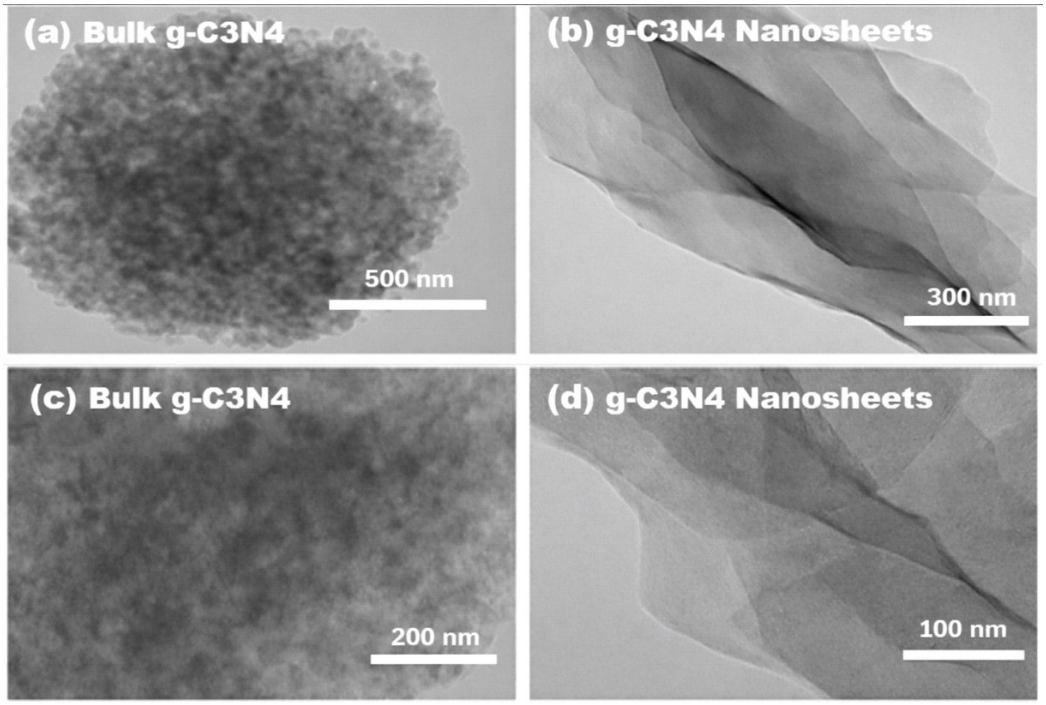

Fig. 7. TEM images of g-C_3N_4. (a,c) Bulk g-C_3N_4 showing dense and aggregated morphology at different magnifications. (b,d) Exfoliated g-C_3N_4 nanosheets exhibiting thin, transparent, and layered sheet-like structures. TEM, transmission electron microscopy. Fig. 7a scale bar = 500 nm.; Fig. 7b scale bar = 300 nm; Fig. 7c scale bar = 200 nm; Fig. 7d scale bar = 100 nm.

Munk function confirms irradiation-induced variations in optical response, which can be attributed to localized structural distortions and enhanced exfoliation effects within the nanosheet architecture. Band gap values derived from Tauc plots indicate the presence of both direct (3.0–3.2 eV) and indirect (2.4–2.8 eV) optical transitions, with irradiated samples exhibiting modest upward shifts relative to the pristine material. These controlled changes in band gap energy suggest that γ-irradiation provides an effective means of tuning the light-harvesting characteristics of g-C_3N_4 nanosheets without compromising their structural integrity. Overall, the results establish γ-irradiation as a versatile strategy for engineering the optical and electronic properties of g-C_3N_4, which is particularly advantageous for applications in photocatalysis, solar energy conversion, and optoelectronic devices where optimized band alignment is critical for performance [29].

3.7.1 Optical Reflection Behavior of γ-Irradiated g-C_3N_4 Nanosheets

Fig. 8 presents the UV–Vis DRS of g-C_3N_4 nanosheets synthesized at 550 °C and subjected to varying γ-irradiation doses (0–50 kGy). All samples exhibit a strong absorption response in the visible region, characteristic of the intrinsic electronic structure of g-C_3N_4. The absorption edge is located around the blue-green region of the spectrum, confirming the suitability of the material for visible-light-driven applications.

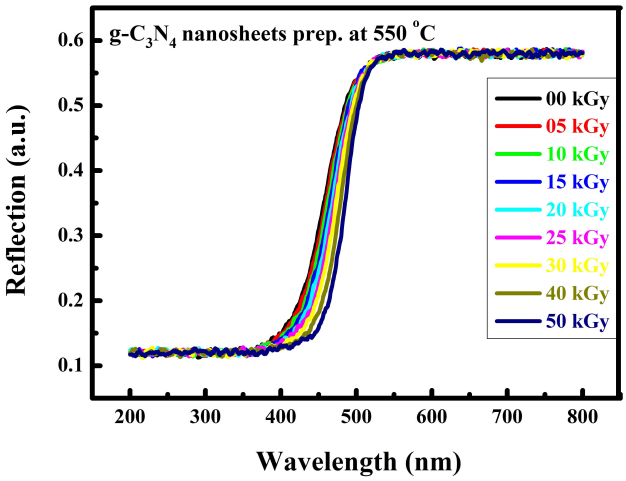

Fig. 8. DRS of g-C_3N_4 nanosheets prepared at 550 °C under different γ-irradiation doses. DRS, diffuse reflectance spectroscopy.

With increasing γ-irradiation dose, a subtle but systematic shift in the absorption edge is observed, accompanied by minor variations in reflectance intensity. These changes suggest irradiation-induced modifications in the electronic structure, which may originate from defect formation, lattice distortion, or altered charge distribution within the g-C_3N_4 framework. Importantly, the overall spectral profile remains well preserved across all irradiation doses, indicating that the fundamental optical charac-

teristics of g-C_3N_4 nanosheets are retained despite irradiation treatment. The controlled tuning of optical absorption through γ-irradiation highlights an effective strategy for tailoring the electronic and light-harvesting properties of g-C_3N_4 nanosheets without compromising their structural integrity, which is advantageous for photocatalytic and optoelectronic applications.

3.7.2 Kubelka–Munk Function Analysis of γ-Irradiated g-C_3N_4 Nanosheets

The optical band structure of γ-irradiated g-C_3N_4 nanosheets was evaluated using the Kubelka–Munk function derived from the UV–Vis DRS. The reflectance data were transformed according to the Kubelka–Munk formalism, enabling a reliable assessment of the absorption behavior and band gap evolution of the material. As shown in Fig. 9, all samples exhibit a well-defined absorption edge in the visible region, confirming the semiconducting nature of g-C_3N_4 nanosheets.

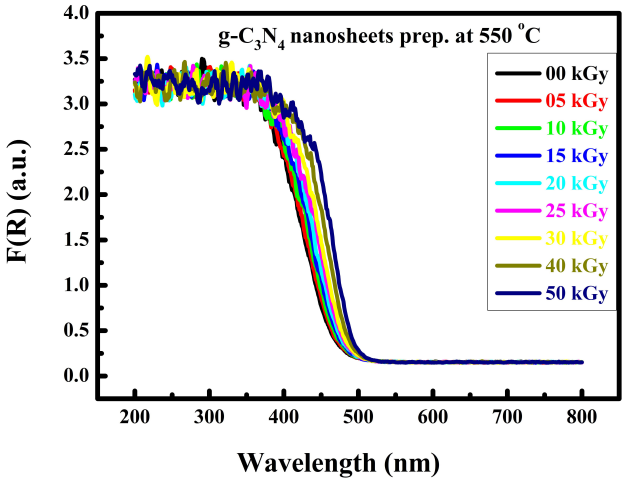

Fig. 9. Effect of γ-irradiation on the Kubelka–Munk function of g-C_3N_4 nanosheets.

With increasing γ-irradiation dose, a gradual shift of the absorption edge toward longer wavelengths is observed, accompanied by subtle variations in reflectance intensity. This behavior indicates irradiation-induced modification of the electronic structure, which can be reasonably attributed to the formation of localized defect states and lattice perturbations within the g-C_3N_4 framework. Importantly, the overall spectral profile remains largely unchanged across the investigated dose range, suggesting that γ-irradiation induces controlled electronic tuning without causing significant structural degradation. Such moderate band structure modulation is advantageous for enhancing visible-light absorption and improving charge carrier utilization, which are critical factors governing the photocatalytic performance of g-C_3N_4-based materials. The optical band structure of γ-irradiated g-C_3N_4 nanosheets was further evaluated using the Kubelka–Munk function derived from UV–Vis DRS. The reflectance data were converted to the corresponding absorption coefficient using the Kubelka–Munk equation (Eqn. 4), which allows reliable estimation of the optical band gap for semiconducting materials [20,30].

3.7.3 Effect of γ-Irradiation on the Optical Absorption of g-C_3N_4 Nanosheets

The UV–Vis absorption spectra of γ-irradiated g-C_3N_4 nanosheets, derived from diffuse reflectance measurements, are presented in Fig. 10. All samples exhibit strong absorption in the near-UV and visible regions, with a well-defined absorption edge characteristic of the semiconducting nature of g-C_3N_4. As the γ-irradiation dose increases, a gradual red shift of the absorption edge is observed, together with slight changes in absorbance intensity.

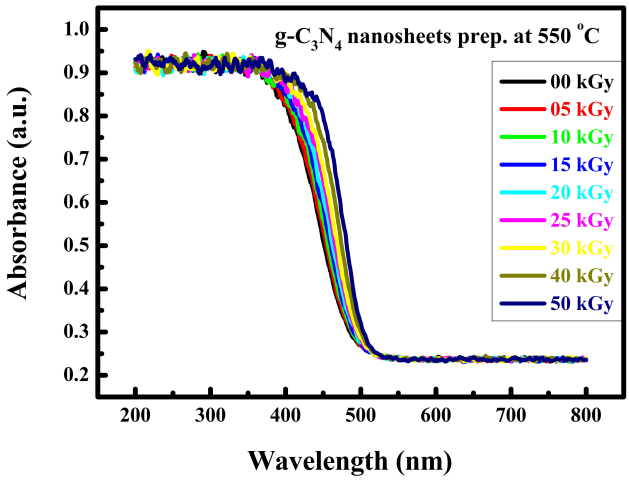

Fig. 10. UV–Vis absorption spectra of g-C_3N_4 nanosheets prepared at 550 °C under different γ-irradiation doses. UV–Vis, ultraviolet–visible.

These spectral variations indicate irradiation-induced modification of the electronic structure, which can be attributed to the formation of localized defect states and subtle lattice distortions within the g-C_3N_4 framework. Importantly, the overall absorption profile remains largely preserved across the investigated dose range, suggesting that γ-irradiation enables controlled tuning of the optical properties without causing significant structural damage. Such moderate enhancement of visible-light absorption is beneficial for improving photoexcited charge generation and is expected to contribute positively to the photocatalytic performance of g-C_3N_4 nanosheets [15,31].

3.7.4 Direct Band Gap Analysis of g-C_3N_4 Nanosheets Under γ-Irradiation

The optical band gap of g-C_3N_4 nanosheets synthesized at 550 °C was evaluated using Tauc plots derived from DRS, as shown in Fig. 11, for samples subjected to

γ-irradiation doses ranging from 0 to 50 kGy. The well-defined linear regions of the Tauc plots indicate that the optical absorption is governed predominantly by direct electronic transitions, from which band gap energies in the range of approximately 3.0–3.2 eV were determined. The pristine g-C_3N_4 nanosheets exhibit a band gap of about 3.0 eV, whereas a gradual increase to nearly 3.2 eV is observed with increasing γ-irradiation dose, evidencing a subtle blue shift in the absorption edge.

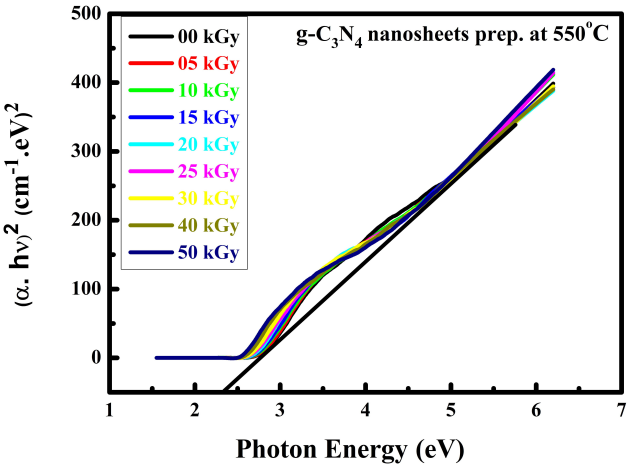

Fig. 11. Tauc plot analysis for direct band gap determination of γ-irradiated g-C_3N_4 nanosheets.

This slight widening of the band gap can be ascribed to irradiation-induced structural distortions and the formation of defect states, which alter the local electronic environment and influence optical transition energies. Importantly, despite these irradiation-induced modifications, the intrinsic semiconducting framework of g-C_3N_4 remains largely preserved, highlighting its structural and electronic robustness under high-dose γ-irradiation. The controlled modulation of the band gap via γ-irradiation thus represents a viable strategy for fine-tuning the optical properties of g-C_3N_4 nanosheets for advanced photocatalytic and optoelectronic applications [28].

3.7.5 Indirect Band Gap Analysis of g-C_3N_4 Nanosheets Under γ-Irradiation

Fig. 12 presents the Tauc plots used to evaluate the indirect optical band gap of g-C_3N_4 nanosheets synthesized at 550 °C and exposed to γ-irradiation doses ranging from 0 to 50 kGy. The indirect band gap energies were determined by extrapolating the linear regions of the $(\alpha h\nu)^{1/2}$ versus photon energy plots. The pristine g-C_3N_4 nanosheets exhibit an indirect band gap of approximately 2.45 eV, while the irradiated samples show a gradual increase to values in the range of 2.4–2.7 eV with increasing irradiation dose. These modest upward shifts in band gap energy suggest that γ-irradiation induces localized structural distortions and defect states that subtly influence the electronic transition pathways without significantly altering the intrinsic band structure of the material. Importantly, the consistent position of the absorption edge across all irradiation doses confirms the robust semiconducting nature and structural stability of g-C_3N_4 under high-dose γ-irradiation. The observed fine-tuning of the indirect band gap highlights γ-irradiation as an effective and controllable strategy for tailoring the optical and electronic properties of g-C_3N_4 nanosheets, which is particularly beneficial for photocatalytic and energy conversion applications where optimized band alignment is critical for performance [29].

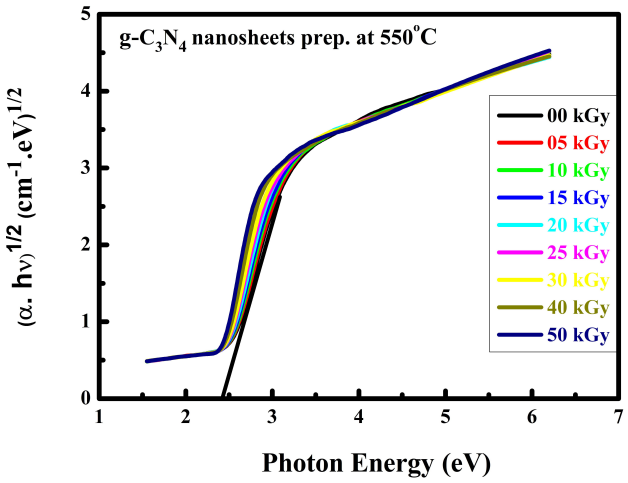

Fig. 12. Indirect band gap estimation of g-C_3N_4 nanosheets at 550 °C derived from Tauc plot analysis under varying γ-irradiation doses.

3.8 Textural Properties of γ-Irradiated g-C_3N_4 Nanosheets

The textural characteristics of g-C_3N_4 nanosheets synthesized at 550 °C were systematically investigated as a function of γ-irradiation dose using nitrogen adsorption–desorption measurements. Key parameters, including specific surface area, total pore volume, and average pore diameter, were analyzed to elucidate the influence of γ-irradiation on the porous architecture of the nanosheets. γ-irradiation is known to induce microstructural modifications through defect generation, partial exfoliation, and disruption of interlayer interactions, which can collectively alter the accessibility and distribution of surface and pore features. The present results demonstrate that controlled γ-irradiation effectively modulates the textural properties of g-C_3N_4 without compromising its structural integrity. The irradiation-induced enhancement of surface area and pore-related parameters is expected to facilitate improved mass transport and increased exposure of catalytically active sites, thereby providing favorable conditions for enhanced photocatalytic performance. Detailed discussions

of the individual contributions of surface area, pore volume, and pore diameter as functions of irradiation dose are presented in the following subsections (Sections 3.8.1–3.8.3).

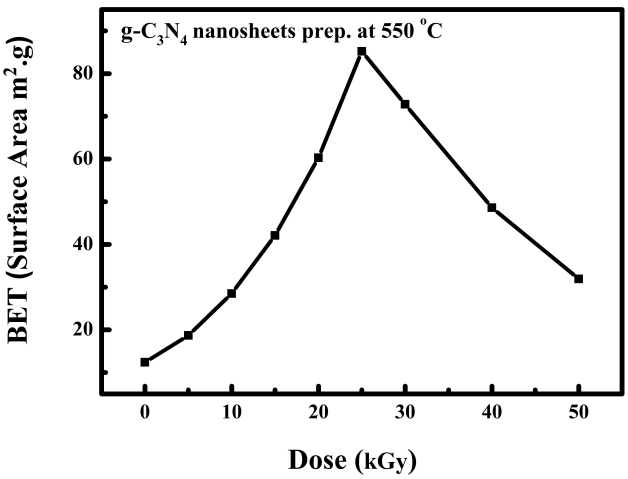

Fig. 13. BET surface area of g-C_3N_4 nanosheets as a function of γ-irradiation dose. BET, Brunauer–Emmett–Teller.

3.8.1 Effect of γ-Irradiation on the Surface Area of g-C_3N_4 Nanosheets

The variation in the BET specific surface area of g-C_3N_4 nanosheets synthesized at 550 °C as a function of γ-irradiation dose is presented in Fig. 13. The pristine sample exhibits a moderate surface area characteristic of layered g-C_3N_4 materials. Upon γ-irradiation, a gradual increase in surface area is observed with increasing dose, reaching a maximum at intermediate irradiation levels before showing a tendency toward saturation at higher doses. This behavior can be attributed to irradiation-induced exfoliation and the generation of microstructural defects, which promote partial delamination of stacked nanosheets and increase the availability of accessible surface sites [30,31]. At higher irradiation doses, the stabilization of surface area suggests a balance between exfoliation and defect recombination or partial structural relaxation. Importantly, no abrupt loss in surface area is detected across the investigated dose range, indicating that the overall framework of g-C_3N_4 remains structurally robust under γ-irradiation. The irradiation-driven enhancement in surface area is expected to be beneficial for photocatalytic applications, as increased surface exposure facilitates improved adsorption of reactant species and more efficient utilization of active sites during photocatalytic reactions.

3.8.2 γ-Irradiation-Induced Modulation of Pore Volume in g-C_3N_4 Nanosheets

Fig. 14 illustrates the variation in total pore volume of g-C_3N_4 nanosheets synthesized at 550 °C as a function of γ-irradiation dose. The pristine sample exhibits a relatively

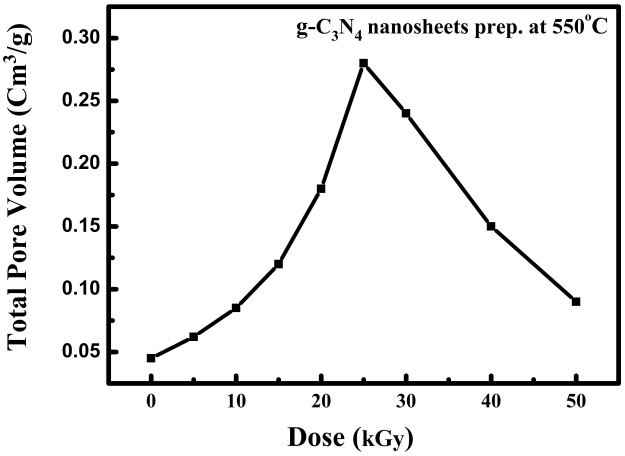

Fig. 14. Total pore volume of g-C_3N_4 nanosheets as a function of γ-irradiation dose.

low pore volume, consistent with the dense stacking typically observed in bulk g-C_3N_4. Upon γ-irradiation, a gradual increase in total pore volume is observed with increasing dose, indicating irradiation-induced microstructural modification. This enhancement is primarily attributed to partial exfoliation, defect formation, and the creation of interlayer voids arising from the disruption of van der Waals interactions between adjacent nanosheets. At higher irradiation doses, the pore volume tends to stabilize, suggesting that a dynamic equilibrium is reached between defect generation and structural relaxation. Importantly, no abrupt collapse or degradation of the porous framework is detected, confirming the structural resilience of g-C_3N_4 under γ-irradiation. The observed increase in pore volume, together with the enhanced surface area, is expected to facilitate improved mass transport and greater accessibility of active sites, which are critical factors for enhancing photocatalytic efficiency and reaction kinetics [29,30].

3.8.3 Impact of γ-Irradiation on the Average Pore Diameter of g-C_3N_4 Nanosheets

Fig. 15 presents the variation in average pore diameter of g-C_3N_4 nanosheets synthesized at 550 °C as a function of γ-irradiation dose. The pristine sample exhibits a relatively small average pore diameter, reflecting the compact stacking and limited interlayer spacing characteristic of non-irradiated g-C_3N_4. With increasing γ-irradiation dose, a gradual enlargement of the average pore diameter is observed, indicating progressive modification of the porous architecture. This behavior can be attributed to irradiation-induced exfoliation and defect formation, which promote partial delamination of the nanosheets and the expansion of interlayer voids. At higher doses, the increase in pore diameter becomes less pronounced, suggesting the establishment of a structural balance between defect generation and framework stabilization [31]. Importantly, the absence of abrupt pore collapse or excessive pore coalescence con-

firms the robustness of the g-C_3N_4 framework under γ-irradiation. The moderate enlargement of pore diameter, combined with enhanced surface area and pore volume, is expected to improve reactant diffusion and active-site accessibility, thereby favorably influencing photocatalytic reaction kinetics and overall performance.

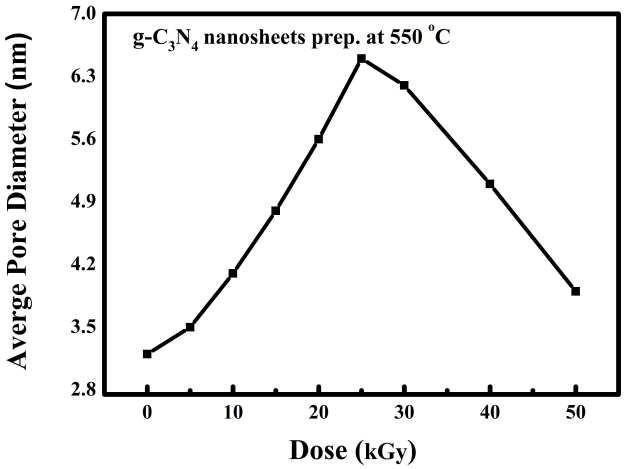

Fig. 15. Average pore diameter of g-C_3N_4 nanosheets as a function of γ-irradiation dose.

3.9 PL Characteristics and Charge-Carrier Dynamics of γ-Irradiated g-C_3N_4 Nanosheets

PL spectroscopy and TRPL measurements were employed to elucidate the influence of γ-irradiation on the electronic structure, defect states, and charge-carrier recombination dynamics of g-C_3N_4 nanosheets synthesized at 550 °C. PL-based analyses provide critical insight into excitonic behavior, radiative and non-radiative recombination pathways, and the role of irradiation-induced defects in governing optical performance. γ-irradiation is known to introduce lattice distortions and defect states of varying depths, which can either enhance or suppress luminescence depending on their nature and concentration. The present results reveal a strong dose-dependent modulation of PL intensity, emission wavelength, and carrier lifetime, highlighting a delicate balance between beneficial shallow defect formation and detrimental deep-level trap generation [31–33]. Moderate γ-irradiation effectively suppresses fast non-radiative recombination, prolongs exciton lifetime, and enhances radiative emission, whereas excessive irradiation induces defect saturation and structural disorder that accelerate carrier quenching. These findings demonstrate that controlled γ-irradiation offers a powerful strategy for tuning the photophysical properties and charge-carrier dynamics of g-C_3N_4 nanosheets, with direct implications for optimizing their performance in photocatalysis, light-harvesting systems, and optoelectronic applications. Detailed discussions of PL intensity evolution, lifetime behavior, decay kinetics, emission wavelength shifts, PL quantum yield variation, Relative PL efficiency and recombination suppression efficiency are provided in the following subsections (Sections 3.9.1–3.9.8).

3.9.1 Photoluminescence Response of g-C_3N_4 Nanosheets Under Different Gamma Irradiation Doses

The PL spectra of g-C_3N_4 nanosheets exhibit a strong dependence on γ-irradiation dose, as illustrated in Fig. 16. The pristine sample (0 kGy) shows a characteristic emission band centered at approximately 455 nm, which gradually intensifies with increasing irradiation dose and reaches a maximum at around 20–25 kGy. This enhancement is mainly attributed to the formation of irradiation-induced shallow defect states, such as nitrogen vacancies and localized lattice distortions, which act as temporary charge-carrier trapping centers.

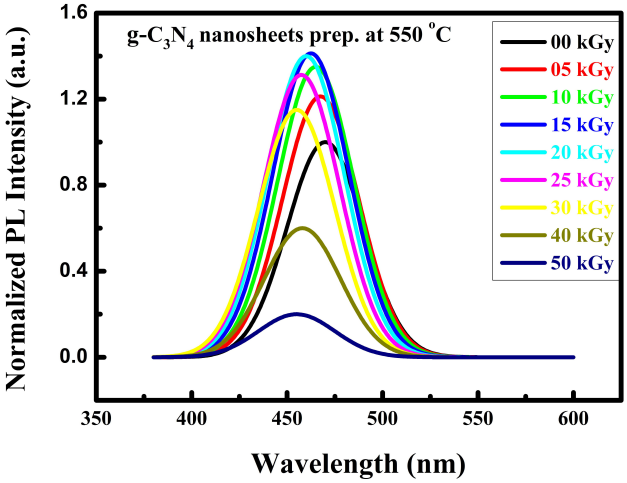

Fig. 16. Normalized PL spectra of g-C_3N_4 nanosheets at varying gamma irradiation doses. PL, Photoluminescence.

These shallow traps promote exciton localization and suppress rapid non-radiative recombination, thereby increasing the probability of radiative transitions. When the γ-irradiation dose exceeds 25 kGy, a pronounced decrease in PL intensity is observed. This behavior indicates the onset of defect saturation and the generation of deep trap states that function as efficient non-radiative recombination centers [32–34]. Excessive irradiation may also induce structural disorder within the conjugated g-C_3N_4 framework, further accelerating carrier quenching and reducing emission efficiency. Overall, these results demonstrate that controlled γ-irradiation provides an effective means to tailor the electronic structure and excitonic recombination behavior of g-C_3N_4 nanosheets, where an optimal balance between beneficial shallow defect formation and structural preservation is essential for maximizing optical performance.

3.9.2 Influence of Gamma Irradiation Dose on the Average Lifetime of g-C_3N_4 Nanosheets

Fig. 17 presents the variation in the average PL lifetime of g-C_3N_4 nanosheets synthesized at 550 °C as a function of γ-irradiation dose. The lifetime displays a clear non-monotonic behavior, initially increasing at low irradiation doses and reaching a pronounced maximum of approximately 4.6 ns at 25 kGy. This enhancement indicates that moderate γ-irradiation introduces a suitable density of shallow defect states, which act as temporary charge-carrier traps and effectively suppress fast non-radiative recombination, thereby prolonging carrier lifetime.

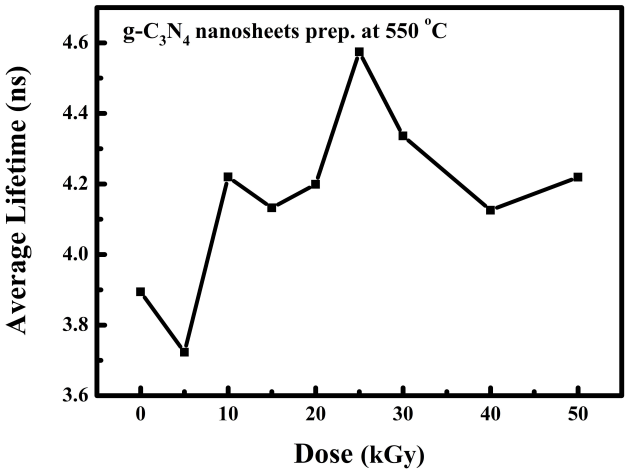

Fig. 17. Variation of average lifetime of g-C_3N_4 nanosheets as a function of gamma irradiation dose.

In contrast, further increasing the irradiation dose beyond 25 kGy results in a noticeable reduction in the average PL lifetime. This decrease is associated with defect saturation and irradiation-induced structural disorder, leading to the formation of deep trap states that facilitate rapid non-radiative recombination. These observations highlight that controlled γ-irradiation plays a crucial role in optimizing charge-carrier dynamics in g-C_3N_4 nanosheets, whereas excessive irradiation adversely affects their optical performance and recombination behavior [32,33].

3.9.3 Dose-Dependent Photoluminescence Intensity of g-C_3N_4 Nanosheets

Fig. 18 illustrates the variation in PL peak intensity of g-C_3N_4 nanosheets synthesized at 550 °C as a function of γ-irradiation dose. The PL intensity initially increases with increasing dose and reaches a maximum at approximately 15–20 kGy. This improvement arises from irradiation-induced shallow defect states, such as nitrogen vacancies and localized lattice distortions, which enhance exciton localization and favor radiative recombination by temporarily trapping charge carriers and suppressing rapid non-radiative processes. In this dose range, defect generation remains well controlled and does not significantly disrupt the conjugated heptazine framework, resulting in improved electronic interactions and enhanced emission intensity. With further increase in γ-irradiation dose beyond 20 kGy, the PL intensity progressively decreases. This decline indicates the onset of defect saturation and the formation of deep trap states that act as efficient non-radiative recombination centers. Excessive irradiation may also induce structural distortions within the g-C_3N_4 network, accelerating carrier quenching and reducing luminescence efficiency. Overall, the observed dose-dependent PL behavior reflects a critical balance between beneficial defect generation and irradiation-induced structural damage, demonstrating that moderate γ-irradiation optimizes the optical performance of g-C_3N_4 nanosheets, whereas higher doses lead to deterioration of their luminescence properties.

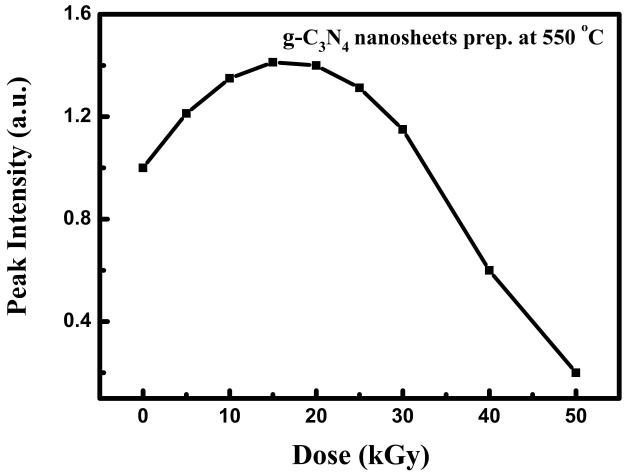

Fig. 18. Variation of PL peak intensity of g-C_3N_4 nanosheets with gamma irradiation dose.

3.9.4 Time-Resolved Photoluminescence Decay of g-C_3N_4 Nanosheets Under Gamma Irradiation

Fig. 19 presents the TRPL decay profiles of g-C_3N_4 nanosheets synthesized at 550 °C and subjected to different γ-irradiation doses [33]. All decay curves display a rapid initial drop in PL intensity followed by a slower decay tail, which is characteristic of multi-exponential recombination behavior involving both radiative and non-radiative processes. This behavior reflects the coexistence of free exciton recombination and defect-assisted carrier trapping within the g-C_3N_4 framework. At low to moderate irradiation doses (5–25 kGy), the decay profiles become slightly prolonged, indicating suppression of fast non-radiative recombination pathways. This effect is attributed to the formation of irradiation-induced shallow defect states that temporarily trap charge carriers, thereby extending exciton lifetime and enhancing radiative recombination probability. In contrast, at higher irradiation doses ($\geq$30 kGy),

the decay curves converge toward shorter lifetimes, suggesting the emergence of deep-level trap states and increased structural disorder. These deep traps act as efficient non-radiative recombination centers, accelerating carrier quenching and diminishing luminescence efficiency. Overall, the TRPL results confirm that moderate γ-irradiation effectively optimizes charge carrier dynamics in g-C_3N_4 nanosheets, whereas excessive irradiation induces unfavorable defect states and structural distortions that compromise recombination behavior and optical performance.

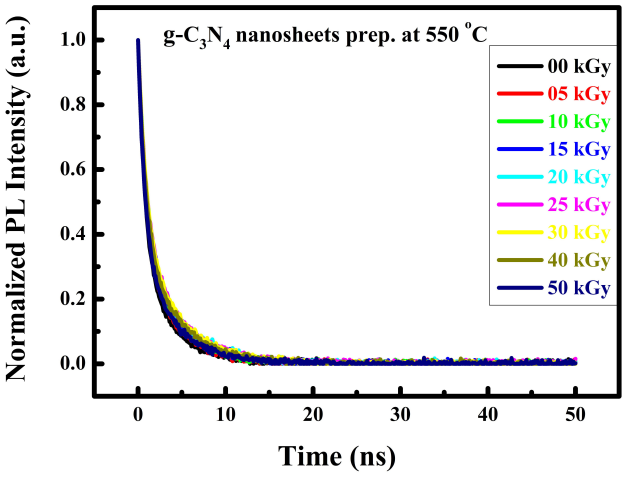

Fig. 19. Normalized PL decay curves of g-C_3N_4 nanosheets at different gamma irradiation doses.

3.9.5 Gamma Irradiation-Dependent Evolution of τ_2 Lifetime in g-C_3N_4 Nanosheets

Fig. 20 shows the dependence of the longer decay component (τ_2) of g-C_3N_4 nanosheets synthesized at 550 °C on γ-irradiation dose. The τ_2 lifetime increases gradually from approximately 3.5 ns for the pristine sample to a maximum value of about 4.4 ns at 25–30 kGy. This prolongation indicates effective suppression of non-radiative recombination pathways and enhanced stabilization of photogenerated charge carriers, which can be attributed to the controlled formation of irradiation-induced shallow defect states that temporarily trap carriers and delay recombination [34]. When the irradiation dose exceeds 30 kGy, the τ_2 lifetime decreases progressively. This reduction reflects the accumulation of irradiation-induced structural disorder and the emergence of deep-level trap states that act as efficient non-radiative recombination centers, thereby accelerating carrier recombination. These results clearly demonstrate the dual role of γ-irradiation in tailoring the photophysical properties of g-C_3N_4 nanosheets and hence moderate irradiation improves exciton lifetime and charge carrier dynamics, while excessive exposure leads to deterioration of optical performance due to defect saturation and structural damage.

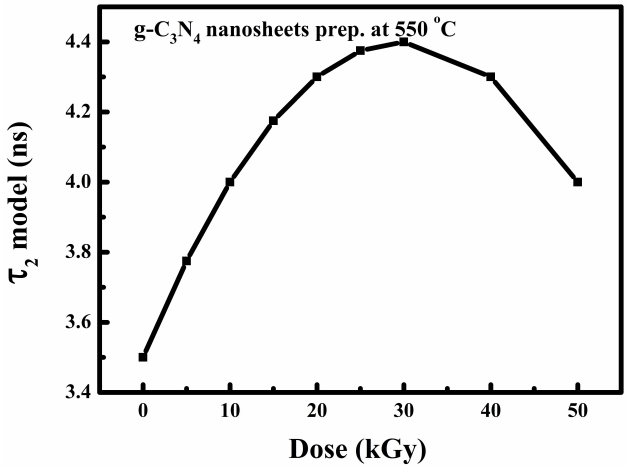

Fig. 20. Variation of τ_2 model lifetime of g-C_3N_4 nanosheets with gamma irradiation dose.

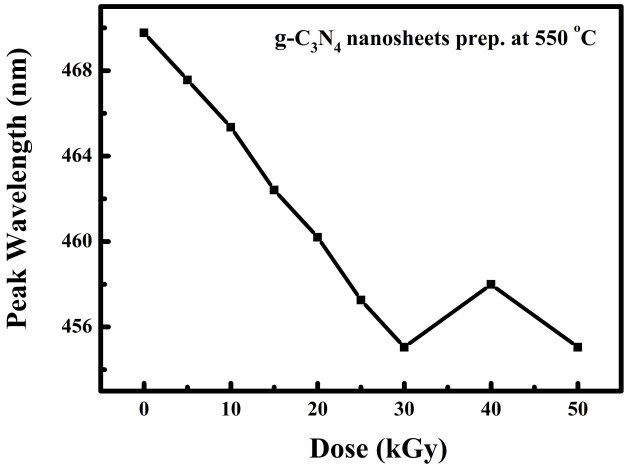

Fig. 21. Variation of PL peak wavelength of g-C_3N_4 nanosheets with gamma irradiation dose.

3.9.6 γ-Irradiation-Induced Shifts in Emission Wavelength of g-C_3N_4 Nanosheets

Fig. 21 illustrates the evolution of the PL emission peak of g-C_3N_4 nanosheets synthesized at 550 °C as a function of γ-irradiation dose. The pristine sample exhibits an emission maximum at approximately 469 nm, whereas the irradiated nanosheets show a pronounced blue-shift to about 456 nm at an irradiation dose of 30 kGy. This blue-shift originates from quantum confinement effects induced by γ-irradiation, arising from nanosheet thinning and localized lattice distortions, which modify the spatial confinement of charge carriers. In addition, irradiation reduces the effective conjugation length and alters defect-related energy levels through the formation of shallow defect states, collectively leading to a widening of the effective bandgap and emission at shorter wavelengths. At higher irradiation doses, a slight red-shift is observed at 40 kGy, followed by a minor blue-shift at 50 kGy, indicating the coexistence of

competing effects related to partial defect passivation and increasing structural disorder. Overall, these systematic variations in emission wavelength demonstrate the strong sensitivity of the electronic structure of g-C_3N_4 nanosheets to γ-irradiation and confirm that controlled radiation exposure provides an effective approach for tuning their optical properties [35].

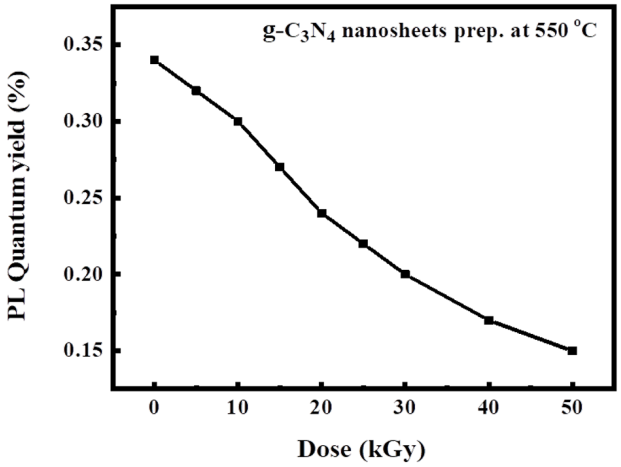

Fig. 22. Variation of PL quantum yield of g-C_3N_4 nanosheets prepared at 550 °C as a function of γ-irradiation dose.

3.9.7 Effect of γ-Irradiation on PL Quantum Yield and Charge Carrier Recombination Behavior of g-C_3N_4 Nanosheets

The influence of γ-irradiation on the radiative recombination behavior of g-C_3N_4 nanosheets was further evaluated through PL quantum yield analysis (Fig. 22). The pristine sample exhibits the highest PL quantum yield, approximately 0.32, indicating a relatively high probability of radiative electron–hole recombination. Upon γ-irradiation, the PL quantum yield decreases progressively with increasing dose, declining to about 0.29–0.26 at intermediate doses and reaching a minimum value of approximately 0.18 at 50 kGy [35,36]. This monotonic reduction signifies an effective suppression of radiative recombination pathways, which can be attributed to irradiation-induced structural or electronic modifications, such as the formation of defect states or trap sites that favor non-radiative charge transfer. At higher doses, the pronounced decrease in PL quantum yield implies substantial inhibition of electron–hole recombination, a feature generally considered beneficial for photocatalytic performance. It should be emphasized that the reported PL quantum yield values are discussed in a comparative sense to illustrate irradiation-induced trends rather than absolute quantum efficiencies. Nonetheless, the clear dose-dependent behavior demonstrates that controlled γ-irradiation provides an effective strategy for tuning charge carrier dynamics in g-C_3N_4 nanosheets.

3.9.8 Dose-Dependent PL Efficiency and Recombination Suppression of γ-Irradiated g-C_3N_4 Nanosheets

Fig. 23 illustrates the effect of γ-irradiation on the relative PL efficiency and PL suppression behavior of g-C_3N_4 nanosheets prepared at 550 °C. The relative PL efficiency, normalized to the pristine sample, decreases gradually with increasing irradiation dose, indicating a progressive reduction in radiative electron–hole recombination. This trend is accompanied by a corresponding increase in PL suppression, which becomes particularly pronounced at higher doses. Such behavior suggests that γ-irradiation induces modifications in the electronic structure of g-C_3N_4 that favor charge carrier separation, likely through the introduction of defect states or trapping centers that facilitate non-radiative pathways. Importantly, these results are discussed comparatively, reflecting relative changes in emission behavior rather than absolute quantum efficiencies [37]. Nevertheless, the inverse relationship between PL efficiency and PL suppression provides clear evidence that controlled irradiation effectively modulates charge carrier recombination dynamics, a feature that is generally advantageous for enhancing photocatalytic performance.

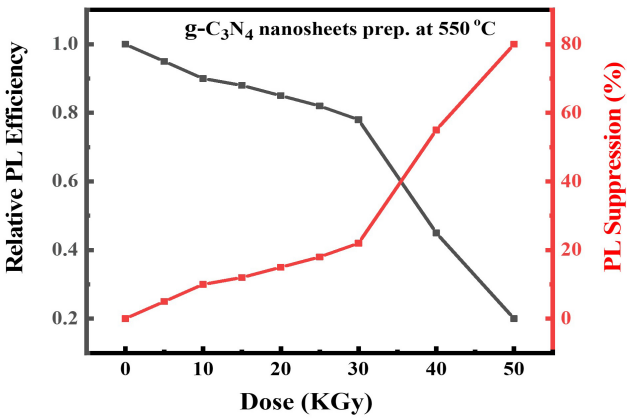

Fig. 23. Relative PL efficiency and PL suppression of g-C_3N_4 nanosheets prepared at 550 °C as a function of γ-irradiation dose.

3.10 Photocatalytic Degradation of MB Using g-C_3N_4 Nanosheets Under γ-Irradiation

This section examines the photocatalytic degradation behavior of methylene blue (initial concentration of 10 mg L^{-1}) over g-C_3N_4 nanosheets synthesized at different calcination temperatures and subjected to varying γ-irradiation doses. A systematic evaluation was conducted by monitoring the time-dependent UV–Vis absorption spectra of MB, assessing the influence of irradiation dose and synthesis temperature on degradation efficiency, analyzing the associated photocatalytic kinetics, and examining both catalytic activity and recyclability. The primary objective was to clarify how the combined effects of synthesis conditions

and γ-irradiation regulate the photocatalytic performance of the prepared g-C_3N_4 nanosheets. The results demonstrate that moderate γ-irradiation doses in the range of 10–25 kGy markedly enhance MB degradation efficiency, which is attributed to the formation of favorable defect states that promote charge separation and prolong the lifetime of photogenerated charge carriers [36]. In contrast, exposure to higher irradiation doses ($\geq$40 kGy) leads to a noticeable deterioration in photocatalytic performance, likely resulting from excessive structural disruption and defect saturation. Synthesis temperature was also found to be a decisive factor, with nanosheets prepared at 550–600 °C exhibiting significantly higher degradation efficiencies than those synthesized at either lower or higher temperatures. Furthermore, stability and recyclability tests reveal that appropriately controlled γ-irradiation not only improves the initial photocatalytic activity but also contributes to maintaining performance over successive reaction cycles. Collectively, these findings underscore the synergistic role of synthesis temperature and γ-irradiation in tailoring the photocatalytic properties of g-C_3N_4 nanosheets for efficient and durable MB degradation.

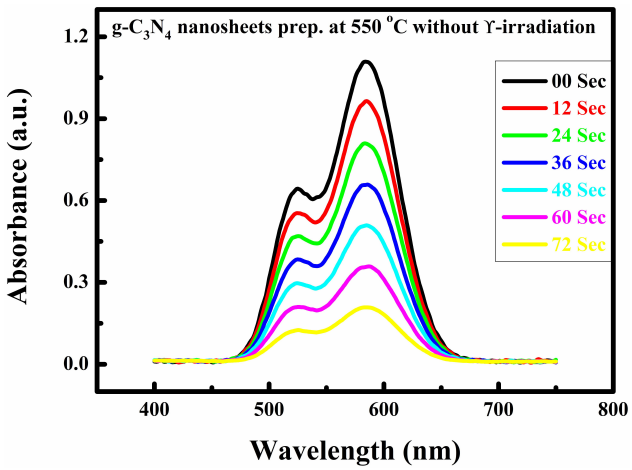

Fig. 24. UV–Vis absorption spectra of MB solution recorded at different irradiation times in the presence of g-C_3N_4 nanosheets prepared at 550 °C under different γ-irradiation doses. MB, methylene blue.

3.10.1 Time-Resolved UV–Vis Absorption of MB Using g-C_3N_4 Nanosheets Without γ-Irradiation

Fig. 24 presents the time-dependent evolution of the UV–Vis absorption spectra of MB during its photocatalytic degradation in the presence of g-C_3N_4 nanosheets synthesized at 550 °C under non-irradiated conditions. The initial MB solution displays a strong absorption band centered at approximately 664 nm, along with a weaker shoulder around 610 nm, both of which are characteristic of the electronic transitions of MB molecules. Upon visible-light irradiation, a progressive decrease in the intensity of these absorption features is observed as the reaction time increases from 0 to 120 minutes, indicating the gradual degradation of the dye. The continuous attenuation of absorbance reflects the effective photocatalytic activity of the g-C_3N_4 nanosheets. During the process, photogenerated charge carriers participate in successive oxidation and reduction reactions, leading to the breakdown of MB into smaller intermediate species and, ultimately, to mineralized products. These results demonstrate the intrinsic photocatalytic capability of non-irradiated g-C_3N_4 nanosheets and provide a reliable reference point for evaluating the performance enhancement achieved through gamma irradiation [36,37].

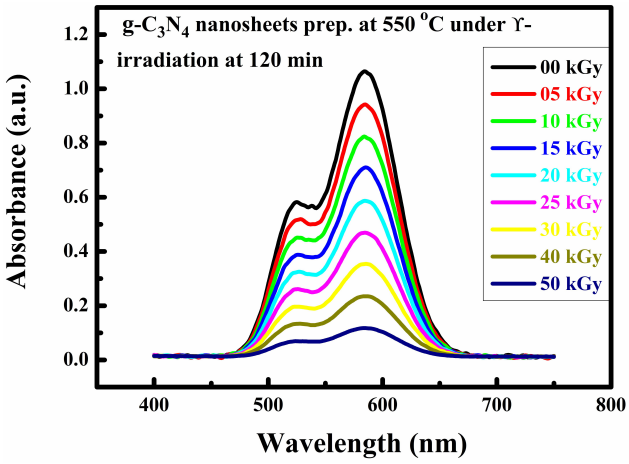

Fig. 25. UV–Vis absorption spectra of MB degradation over g-C_3N_4 nanosheets (550 °C) under different γ-Irradiation at 120 min.

3.10.2 Effect of γ-Irradiation Dose on the Photocatalytic Degradation of MB Over g-C_3N_4 Nanosheets

Fig. 25 illustrates the UV–Vis absorption spectra of the MB solution after 120 min of photocatalytic treatment over g-C_3N_4 nanosheets synthesized at 550 °C and exposed to different γ-irradiation doses. The pristine MB solution exhibits its characteristic main absorption band centered at approximately 664 nm, accompanied by a weaker shoulder around 610 nm, which are typical signatures of the chromophoric structure of MB [36]. Upon photocatalytic treatment in the presence of g-C_3N_4, a progressive attenuation of these absorption features is observed, with the extent of intensity reduction strongly dependent on the applied irradiation dose. In particular, nanosheets subjected to moderate γ-irradiation doses in the range of 10–25 kGy show the most pronounced decrease in MB absorbance, indicating enhanced photocatalytic degradation efficiency. This improvement can be reasonably attributed to irradiation-induced defect states that facilitate charge separation and increase the availability of active sites without severely disrupting the material framework. In contrast, samples ex-

posed to higher irradiation doses (≥40 kGy) retain relatively stronger absorption bands after irradiation, suggesting a decline in degradation efficiency, which is likely associated with defect saturation and partial structural deterioration of the nanosheets. Overall, these results demonstrate that controlled γ-irradiation plays a beneficial role in promoting the photocatalytic degradation of MB, whereas excessive irradiation adversely affects performance.

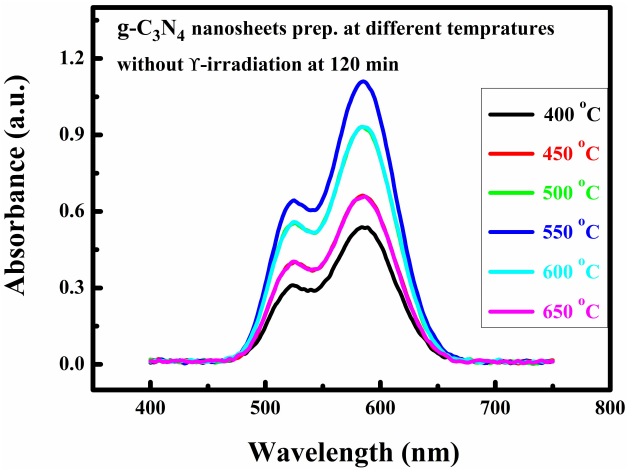

Fig. 26. UV–Vis absorption spectra of MB degradation over g-C_3N_4 nanosheets synthesized at different temperatures without γ-irradiation after 120 min.

3.10.3 Effect of Preparation Temperature on the Photocatalytic Degradation of MB in the Absence of γ-Irradiation

Fig. 26 depicts the UV–Vis absorption spectra of the MB solution after 120 min of photocatalytic treatment using g-C_3N_4 nanosheets synthesized at different preparation temperatures in the absence of γ-irradiation. The residual MB solution exhibits a characteristic absorption band centered at approximately 664 nm, accompanied by a weaker shoulder at lower wavelengths, reflecting incomplete dye degradation under suboptimal catalytic conditions. A clear dependence on synthesis temperature is evident from the variation in absorbance intensity [22,37]. Nanosheets prepared at 550 °C display the lowest residual absorbance, indicating the highest photocatalytic degradation efficiency among the examined samples. Samples synthesized at 600 °C also show relatively strong degradation performance, albeit slightly inferior to that of the 550 °C sample. In contrast, materials prepared at lower temperatures (400–450 °C) retain higher absorbance intensities, suggesting reduced photocatalytic activity, which can be reasonably attributed to incomplete condensation and limited structural development of the g-C_3N_4 framework. Meanwhile, the sample synthesized at 650 °C exhibits diminished degradation efficiency, likely resulting from partial structural deterioration and loss of active sites at excessive calcination temperatures. Overall, these results demonstrate that synthesis temperature plays a critical role in determining the photocatalytic performance of g-C_3N_4 nanosheets, with an optimal preparation window centered around 550 °C under non-irradiated conditions.

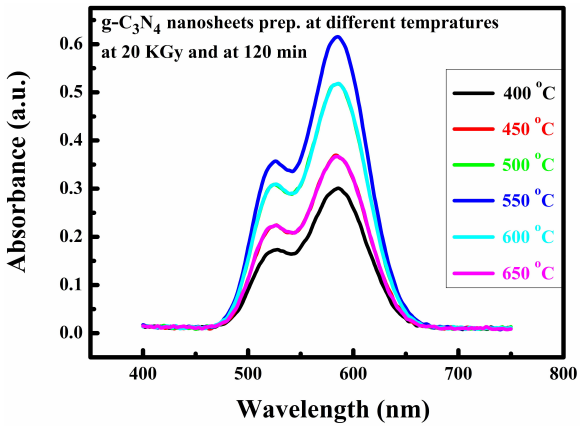

Fig. 27. UV–Vis absorption spectra of MB degradation over g-C_3N_4 nanosheets synthesized at different temperatures after 120 min and under 20 kGy γ- irradiation.

3.10.4 Effect of Synthesis Temperature on the Photocatalytic Degradation of MB Under 20 kGy γ-Irradiation After 120 min

Fig. 27 displays the UV–Vis absorption spectra of the MB solution after 120 min of photocatalytic treatment over g-C_3N_4 nanosheets synthesized at different temperatures and subjected to γ-irradiation at a dose of 20 kGy. For all samples, the characteristic MB absorption band centered near 664 nm is markedly attenuated compared with the non-irradiated condition, confirming that γ-irradiation enhances the overall photocatalytic degradation process. A pronounced dependence on synthesis temperature is clearly observed. In particular, nanosheets prepared at 550 °C exhibit the lowest residual absorbance intensity, indicating the most efficient MB degradation under irradiated conditions [37,38]. Samples synthesized at 600 °C also demonstrate relatively high photocatalytic activity, although slightly inferior to that of the 550 °C sample. By contrast, materials prepared at lower temperatures (400–450 °C) retain higher absorbance levels, reflecting weaker degradation efficiency, which can be attributed to incomplete polymerization and suboptimal structural development of the g-C_3N_4 framework. Similarly, the sample synthesized at 650 °C shows reduced performance, likely due to partial structural degradation and excessive defect formation induced at elevated calcination temperatures. Overall, these results demonstrate that, under moderate γ-irradiation, synthesis temperature plays a decisive role in governing photocatalytic efficiency, with an optimal preparation window centered around 550–600 °C [38].

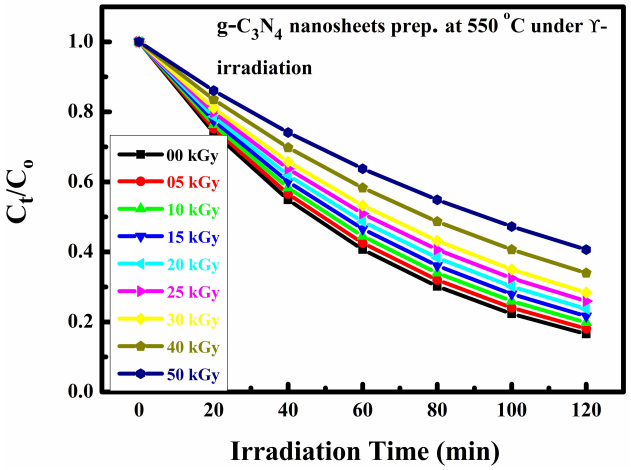

Fig. 28. Degradation profiles of MB (C_t/C_0) over g-C_3N_4 nanosheets synthesized at 550 °C under varying γ-irradiation.

3.10.5 Photocatalytic Degradation Kinetics of MB Over g-C_3N_4 Nanosheets Under Different γ-Irradiation Doses

Fig. 28 illustrates the photocatalytic degradation kinetics of MB over g-C_3N_4 nanosheets synthesized at 550 °C and subjected to different γ-irradiation doses under visible-light illumination. For all investigated samples, the normalized concentration ratio (C_t/C_0) decreases progressively with irradiation time, confirming continuous and effective photocatalytic degradation of MB throughout the reaction period. A pronounced dependence on γ-irradiation dose is evident. Nanosheets treated with moderate irradiation doses (10–25 kGy) exhibit a more rapid decline in C_t/C_0, indicating enhanced degradation kinetics and improved photocatalytic efficiency. This behavior can be reasonably attributed to the introduction of irradiation-induced defect states that facilitate charge carrier separation and migration while preserving the structural integrity of the g-C_3N_4 framework. In contrast, samples exposed to higher irradiation doses ($\geq$40 kGy) show a comparatively slight decrease in C_t/C_0, suggesting suppressed photocatalytic activity, which is likely associated with excessive defect formation and the emergence of charge-recombination centers. The non-irradiated sample displays intermediate kinetic behavior, highlighting the beneficial yet dose-dependent role of γ-irradiation. Overall, these results demonstrate that controlled γ-irradiation at moderate doses effectively optimizes the photocatalytic degradation kinetics of MB, whereas excessive irradiation adversely affects the activity of g-C_3N_4 nanosheets [39].

3.10.6 Degradation Efficiency of MB Over g-C_3N_4 Nanosheets Under Different γ-Irradiation

Fig. 29 illustrates the photocatalytic degradation efficiency of MB as a function of irradiation time over g-C_3N_4 nanosheets synthesized at 550 °C and exposed to different γ-irradiation doses under visible-light illumination. For all samples, the degradation efficiency increases steadily with irradiation time, confirming the continuous and effective photocatalytic removal of MB during the reaction process. A pronounced dependence on γ-irradiation dose is observed. Nanosheets treated with moderate irradiation doses (10–25 kGy) exhibit the highest degradation efficiencies throughout the reaction period, reaching markedly higher removal percentages after 120 min compared with the pristine sample. This enhancement can be reasonably attributed to irradiation-induced defect states that improve charge carrier separation and utilization while maintaining the structural integrity of the g-C_3N_4 framework. In contrast, samples exposed to higher irradiation doses ($\geq$40 kGy) display noticeably lower degradation efficiencies, indicating that excessive defect formation and partial structural disruption adversely affect photocatalytic performance [38]. The non-irradiated sample shows intermediate behavior, highlighting the beneficial yet dose-dependent influence of γ-irradiation. Overall, these results demonstrate that controlled γ-irradiation at moderate doses significantly enhances the photocatalytic degradation efficiency of MB, whereas excessive irradiation diminishes the activity of g-C_3N_4 nanosheets.

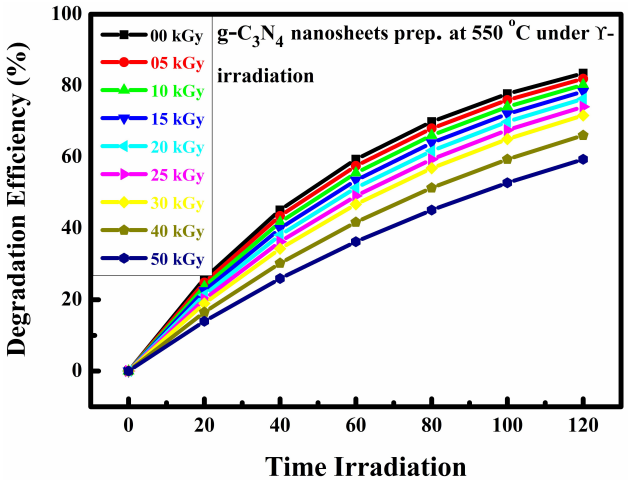

Fig. 29. Degradation efficiency of MB over g-C_3N_4 nanosheets under different gamma irradiation doses.

3.10.7 Identification of Dominant Reactive Species During Photocatalytic Degradation

To clarify the contribution of the main reactive species involved in the photocatalytic degradation of MB, scavenger experiments were carried out under visible-light irradiation, and the results are summarized in Fig. 30. In the absence of scavengers, the γ-irradiated g-C_3N_4 nanosheets exhibit a clear dependence of photocatalytic performance on irradiation dose, with the degradation efficiency increasing up to an intermediate dose and subsequently declining at higher doses. This behavior suggests that γ-irradiation modifies the photocatalytic activity without fundamentally

altering the reaction pathway. Upon the addition of p-benzoquinone (BQ), a pronounced suppression of degradation efficiency is observed across the entire irradiation dose range, indicating that superoxide radicals ($\bullet O_2^-$) play a dominant role in the photocatalytic degradation process. The introduction of PA also leads to a noticeable decrease in photocatalytic activity, though less severe than that induced by BQ, implying that hydroxyl radicals (•OH) contribute as secondary oxidative species. In contrast, the presence of EDTA results in a comparatively moderate reduction in degradation efficiency, suggesting a less dominant but still measurable involvement of photogenerated holes (h^+).

Importantly, the relative suppression trends induced by the different scavengers remain consistent across all γ-irradiation doses, indicating that γ-irradiation primarily influences charge separation efficiency and surface reactivity rather than introducing a new photocatalytic mechanism. The predominance of $\bullet O_2^-$ radicals is consistent with the electronic structure of g-C_3N_4, whose conduction band position favors the reduction of dissolved oxygen under visible-light excitation. Overall, the scavenger results provide experimental support for the proposed photocatalytic pathway and demonstrate that γ-irradiation acts as an effective strategy to tune the photocatalytic efficiency of g-C_3N_4 nanosheets without altering the fundamental degradation mechanism.

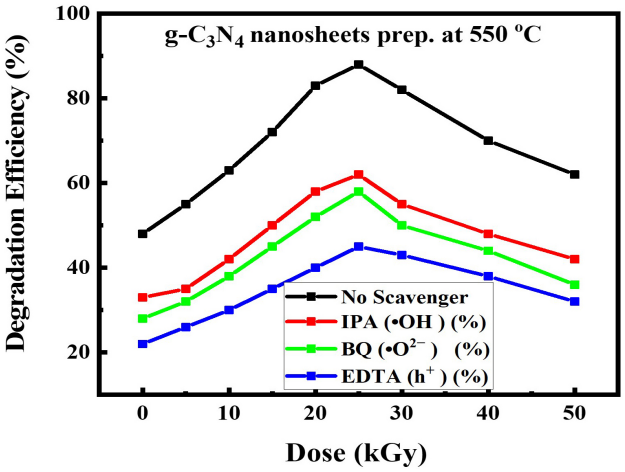

Fig. 30. Effect of reactive species scavengers on the photocatalytic degradation of MB over γ-irradiated g-C_3N_4 nanosheets.

3.10.8 Stability and Recyclability of g-C_3N_4 Nanosheets in MB Photodegradation Under γ-Irradiation

Fig. 31 presents the variation of the apparent pseudo-first-order rate constant (k_{app}) for MB degradation over γ-irradiated g-C_3N_4 nanosheets as a function of successive photocatalytic cycles. For all samples, a gradual decline in the rate constant is observed with increasing cycle number, indicating partial deactivation of the photocatalyst during repeated use. Nevertheless, nanosheets exposed to moderate γ-irradiation doses (10–25 kGy) consistently exhibit higher rate constants throughout the cycling tests compared with the pristine material, confirming their superior and more stable photocatalytic activity [39,40]. The enhanced performance at these doses can be attributed to an optimized defect structure that promotes efficient charge carrier separation while preserving the integrity of the g-C_3N_4 framework. In contrast, samples irradiated at higher doses ($\geq$40 kGy) display significantly lower rate constants and a more pronounced decline upon reuse, suggesting that excessive irradiation induces structural disorder and non-productive recombination centers. Despite the observable decrease in activity over repeated cycles, the overall trends demonstrate that controlled γ-irradiation at appropriate doses improves both the photocatalytic efficiency and the reusability of g-C_3N_4 nanosheets, whereas over-irradiation is detrimental to long-term performance [41].

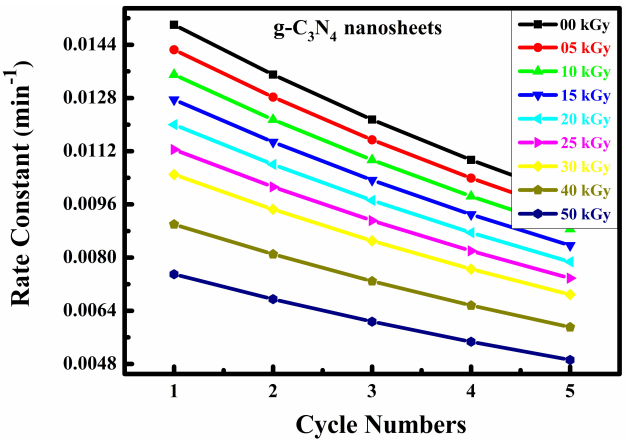

Fig. 31. Apparent rate constants of MB degradation over g-C_3N_4 nanosheets at different γ-irradiation doses across successive cycles.

3.10.9 Cycling Stability and Retention of Photocatalytic Kinetics in γ-Irradiated g-C_3N_4 Nanosheets

The cycling stability of the prepared g-C_3N_4 nanosheets was systematically assessed by tracking the retention of the apparent first-order rate constant (k_n/k_1) over successive photocatalytic runs, as illustrated in Fig. 32. Across all samples, a slight but progressive reduction in k_n/k_1 is observed with increasing cycle number, which can reasonably be attributed to minor catalyst loss during recovery, partial surface coverage by residual intermediates, and gradual attenuation of accessible active sites. Importantly, the overall decrease remains limited, indicating that the structural integrity and intrinsic photocatalytic functionality of g-C_3N_4 are largely maintained throughout repeated use. In comparison with

the pristine material, the γ-irradiated samples—particularly those treated at moderate doses—exhibit noticeably higher retention of the apparent rate constant, reflecting improved resistance to deactivation under cyclic operation. This enhanced stability is plausibly linked to irradiation-induced modifications of the electronic structure and surface states, which promote more robust charge separation while mitigating irreversible surface deterioration. Collectively, these findings are regarding catalyst durability and confirm that controlled γ-irradiation offers a viable strategy for improving both the activity and long-term reusability of g-C_3N_4-based photocatalysts [41].

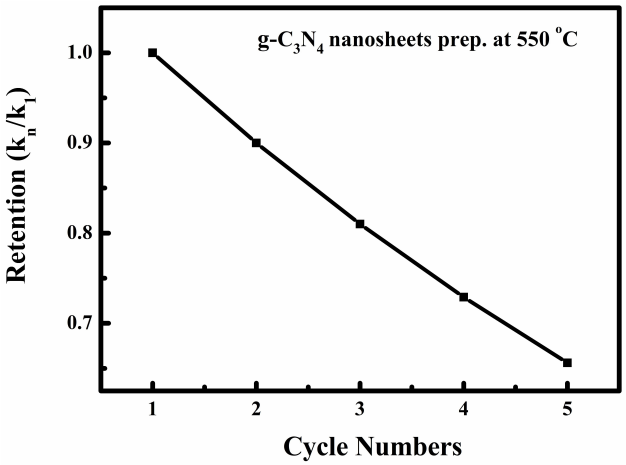

Fig. 32. Retention of apparent first-order rate constant (k_n/k_1) of γ-irradiated g-C_3N_4 nanosheets over successive photocatalytic cycles for MB degradation.

4. Discussion

4.1 Interpretation of Structural Changes Induced by γ-Irradiation

As shown in Table 1, the apparent crystallite size of bulk g-C_3N_4 decreases gradually with increasing irradiation dose, while the corresponding microstrain and dislocation density increase systematically. This trend indicates progressive accumulation of irradiation-induced lattice distortions and defect sites, without evidence of phase transformation or long-range structural disruption, as further supported by the absence of peak shifts or secondary diffraction features in Fig. 2a. In the case of exfoliated g-C_3N_4 nanosheets (Fig. 2b and Table 2), the calculated crystallite sizes are consistently smaller and the microstrain values higher than those of the bulk material at all irradiation doses, reflecting reduced interlayer coherence associated with the exfoliation process. With increasing γ-irradiation dose, both microstrain and dislocation density show a further incremental increase, while the characteristic g-C_3N_4 diffraction peaks remain preserved, confirming that the fundamental crystalline framework is maintained up to 50 kGy.

4.2 Discussion of Photocatalytic Activity

In contrast, samples exposed to higher irradiation doses ($\geq$40 kGy) display noticeably lower degradation efficiencies, indicating that excessive defect formation and partial structural disruption adversely affect photocatalytic performance. The non-irradiated sample shows intermediate behavior, highlighting the beneficial yet dose-dependent influence of γ-irradiation. Overall, these results demonstrate that controlled γ-irradiation at moderate doses significantly enhances the photocatalytic degradation efficiency of MB, whereas excessive irradiation diminishes the activity of g-CN_4 nanosheets.

4.3 Discussion of Reactive Species Mechanism

To clarify the contribution of the main reactive species involved in the photocatalytic degradation of MB, scavenger experiments were carried out under visible-light irradiation. Upon the addition of p-benzoquinone, a pronounced suppression of degradation efficiency is observed, indicating that superoxide radicals ($\bullet O_2^-$) play a dominant role in the photocatalytic degradation process. The introduction of isopropyl alcohol also leads to a noticeable decrease in photocatalytic activity, implying that hydroxyl radicals ($\bullet$OH) contribute as secondary oxidative species, while EDTA indicates participation of photogenerated holes (h^+).

4.4 Discussion of Catalyst Stability

Across all samples, a slight but progressive reduction in the apparent rate constant is observed during successive photocatalytic cycles. Nevertheless, nanosheets exposed to moderate γ-irradiation doses exhibit higher rate constants and improved resistance to deactivation, confirming enhanced photocatalytic durability.

4.5 Limitations

The scope of the present study is confined to controlled laboratory conditions and batch-scale experiments, which may not fully represent the behavior of the synthesized g-C_3N_4 nanosheets under practical environmental or industrial wastewater treatment scenarios. Photocatalytic performance was assessed exclusively using MB as a single model contaminant; consequently, the applicability of the findings to more complex or multi-component pollutant systems has not yet been established. In addition, although γ-irradiation and thermal treatments were systematically implemented, the lack of in situ or operando characterization restricts direct insight into dynamic structural, electronic and surface-state evolution during irradiation and photocatalytic processes. Furthermore, long-term durability, reusability under continuous operating conditions, and performance stability over extended cycles were not thoroughly evaluated. Accordingly, future studies should focus on investigations involving real wastewater matrices, continuous-flow systems, extended stability testing, and ad-

vanced in situ analytical techniques to more comprehensively validate the practical applicability of the proposed photocatalytic system.

5. Conclusions

In this study, g-C_3N_4 nanosheets were successfully synthesized through electrochemical exfoliation and subsequently tailored by controlled γ-irradiation over a wide dose range (0–50 kGy). Structural investigations confirmed that γ-irradiation did not disrupt the fundamental g-C_3N_4 framework, while inducing progressive microstructural refinement, evidenced by a reduction in crystallite size from ~24.6 to ~18.4 nm and a corresponding increase in lattice microstrain from 2.05×10^{-3} to 2.68×10^{-3}. Optical analyses revealed dose-dependent band gap modulation, with direct transitions shifting from ~3.0 to ~3.2 eV and indirect band gaps spanning from ~2.4 to ~2.7 eV.

Photoluminescence and time-resolved measurements demonstrated that moderate γ-irradiation effectively suppresses non-radiative recombination, yielding a maximum carrier lifetime of approximately 4.6 ns at an optimal dose of ~25 kGy. In addition, γ-irradiation enhanced surface area and pore characteristics, thereby improving reactant accessibility and mass transport. These synergistic structural and photophysical modifications led to a pronounced enhancement in the visible-light photocatalytic degradation of methylene blue, which followed pseudo-first-order reaction kinetics.

Overall, the findings establish γ-irradiation as a robust and contamination-free strategy for fine-tuning the properties of g-C_3N_4 nanosheets. The combined exfoliation–irradiation approach presented here offers a viable pathway for designing efficient metal-free photocatalysts with improved charge-carrier utilization and photocatalytic performance.

Availability of Data and Materials

The datasets generated and analyzed in the present study can be made available by the corresponding author upon reasonable request.

Author Contributions

AM conceived and designed the study, conducted the principal experimental work, performed data analysis and interpretation, and prepared the original manuscript. MI and HY contributed to the experimental work, data analysis, and discussion of the results. AA contributed to the interpretation of the results and revision of the manuscript. All authors contributed to critical revision of the manuscript for important intellectual content. All authors reviewed and approved the final version of the manuscript. All authors have participated sufficiently in the work and agreed to be accountable for all aspects of the work.

Ethics Approval and Consent to Participate

Not applicable.

Acknowledgment

The authors acknowledge the Physics Department, Faculty of Science, Suez University, P.O. Box 43221, Suez, Egypt, for providing the facilities and technical support necessary to carry out this research. The authors also gratefully acknowledge E. R. Shaaban for valuable scientific discussions and support.

Funding

This research received no external funding.

Conflict of Interest

The authors declare no conflict of interest.

Declaration of AI and AI-assisted Technologies in the Writing Process

During the preparation of this work, the authors used ChatGPT-3.5 to improve language clarity and readability. The authors take full responsibility for the content of the publication.

References

[1] de Quadro Carvalho FD, Gomes-da-Silva NC, de Souza JI, Baracho PH, Freire TM, Xavier LN, *et al*. Pharmacokinetic analysis of ultrathin g-C_3N_4 nanosheets via acid exfoliation. Surfaces and Interfaces. 2025; 72: 107223. https://doi.org/10.1016/j.surfin.2025.107223.

[2] Abbas N, Kim TH. Cubic Cu_2O-decorated B-doped g-C_3N_4 nanosheets for ultrasensitive electrochemical detection of metol. Journal of Environmental Chemical Engineering. 2025; 13: 118489. https://doi.org/10.1016/j.jece.2025.118489.

[3] Mallika B, Nagaraja K, Arunpandian M, Oh TH. Photocatalytic and antimicrobial activity of gum Karaya polymer-g-C_3N_4 nanosheets reinforced ZnO/SiO_2 hydrogel for azo dyes degradation and environmental toxicity evaluation. International Journal of Biological Macromolecules. 2025; 320: 145779. https://doi.org/10.1016/j.ijbiomac.2025.145779.

[4] Ostovar A, Tarkhani M, Mousavi SA, Asadollahi M. Surface modification of GO/PVDF composite membranes using MXene/protonated g-C_3N_4 nanosheet hybrids with enhanced dye separation and antifouling properties. Polymer Engineering & Science. 2024; 64: 565–576. https://doi.org/10.1002/pen.26566.

[5] Zhang R, Wang L, An C, Zhang S, Zhang Y, Wang Y, *et al*. Precursor-reforming strategy to hierarchical porous g-C_3N_4 with nitrogen defects for enhanced visible-light-driven hydrogen evolution. International Journal of Hydrogen Energy. 2024; 84: 731–738. https://doi.org/10.1016/j.ijhydene.2024.08.236.

[6] Lee JH, Jeong SY, Son YD, Lee SW. Facile Fabrication of TiO_2 Quantum Dots-Anchored g-C_3N_4 Nanosheets as 0D/2D Heterojunction Nanocomposite for Accelerating Solar-Driven Photocatalysis. Nanomaterials. 2023; 13: 1565. https://doi.org/10.3390/nano13091565.

[7] Mathur N, Pachar K, Ankita A, Yadav A, Roy P, Gupta P. Interfacial electrochemistry of graphitic carbon nitride nanosheets and polymelamine nanofilms toward integrated sensing and energy platforms. Electrochimica Acta. 2025; 11: 147131. https://doi.org/10.1016/j.electacta.2025.147131.

[8] Amasegowda A, Alkanad K, Al-Zaqri N, Al-khawlani A, Kumar AU, Al-Maswari BM, *et al*. Enhanced photocatalytic H_2 production over p–n S-scheme heterojunctions of $Ni_3V_2O_8$ quantum dots decorated on ultrathin g-C_3N_4 nanosheets. Journal of Environmental Chemical Engineering. 2024; 12: 111841. https://doi.org/10.1016/j.jece.2023.111841.

[9] Morsy A, Toderas M, El-marghany A, Rana D, Abdelaty M, Shokry F, *et al*. Oxygen/g-C_3N_4 smart nanocoatings for sustainable maintenance and sacrificial anode protection of mild steel. Journal of Chemical Technology & Biotechnology. 2025; 100: 187–201. https://doi.org/10.1002/jctb.7764.

[10] Iqbal S, Liu J. S-scheme synergies in Au nanorod-infused Fe_2O_3 quantum dots/g-C_3N_4 hybrids for visible-light-driven water splitting. Journal of Environmental Chemical Engineering. 2024; 12: 114866. https://doi.org/10.1016/j.jece.2024.114866.

[11] Hajizadeh-Oghaz M, Heydari G. Synthesis and characterization of sulfur-doped g-C_3N_4 nanosheets for enhanced photocatalytic removal of organic pollutants. Journal of Advanced Materials in Engineering. 2025; 45: 33–48. https://doi.org/10.47176/jame.45.1.1132.

[12] Chen M, Nie X, Gao W, Shang N, Zhou X, Gao S. Visible-light-driven selective C–H bond oxidation using lead-free $Cs_2AgBiBr_6$/g-C_3N_4 perovskite composites. Inorganic Chemistry Communications. 2025; 182: 115445. https://doi.org/10.1016/j.inoche.2025.115445.

[13] Pandi K, Kangeyan KP, Lakhera SK, Kiong TS, Bernaurdshaw N. Melem hydrate-derived g-C_3N_4 microrods coordinated with Cu^{2+}: Understanding the superior cocatalytic role of copper. Materials Today Sustainability. 2024; 27: 100942. https://doi.org/10.1016/j.mtsust.2024.100942.

[14] Nejat R, Zandi S. Visible-light-responsive $La_{0.7}Sr_{0.3}MnO_3$@TiO_2/g-C_3N_4 nanocomposites for photocatalytic antibiotic degradation and bioactivity applications. Journal of Alloys and Compounds. 2025; 1036: 181866. https://doi.org/10.1016/j.jallcom.2025.181866.

[15] Senthil P, Sankar A, Paramasivaganesh K, Saravanan SP. Enhanced photocatalytic H2 evolution on g-C3N4 nanosheets loaded Au/Zn3(PO4)2 as cocatalysts. Journal of Materials Science: Materials in Electronics. 2025; 36: 1438. https://doi.org/10.1007/s10854-025-15306-9.

[16] Wang Y, Wang X, Antonietti M. Polymeric graphitic carbon nitride as a heterogeneous organocatalyst: From photochemistry to multipurpose catalysis. Angewandte Chemie International Edition. 2012; 51: 68–89. https://doi.org/10.1002/anie.201101182.

[17] Zhang J, Chen Y, Wang X. Two-dimensional covalent carbon nitride nanosheets: Synthesis, functionalization, and applications. Energy & Environmental Science. 2015; 8: 3092–3108. https://doi.org/10.1039/C5EE01895A.

[18] Rajasekaran S, Elumalai A, Sivapriya J, Vasanthan S. Synergistic Design of Al2O3@g-C3N4 hybrid nanocomposite photocatalyst from Tinospora cordifolia Plant extract: A Sustainable Solution for Emerging Organic Pollutants. Ionics. 2025; 31: 9919–9933. https://doi.org/10.1007/s11581-025-06531-7.

[19] Zhang Y, Liu J, Wu G, Chen W. Effect of gamma irradiation on the structure and photocatalytic performance of g-C_3N_4. Radiation Physics and Chemistry. 2016; 122: 1–7. https://doi.org/10.1016/j.radphyschem.2016.01.021.

[20] Dong F, Zhao Z, Xiong T, Ni Z, Zhang W, Sun Y, *et al*. In situ construction of g-C_3N_4/g-C heterojunction for enhanced visible-light photocatalytic activity toward organic pollutants degradation. ACS Applied Materials & Interfaces. 2013; 5: 11392–11401. https://doi.org/10.1021/am403653a.

[21] Kralchevska R, Milanova M, Tsvetkov M, Dimitrov D, Todorovsky D. Influence of gamma irradiation on the photocatalytic activity of Degussa P25 TiO_2. Journal of Materials Science. 2012; 47: 4936–4945. https://doi.org/10.1007/s10853-012-6368-4.

[22] Lamo MB, Williams P, Reece P, Lumpkin GR, Sheppard LR. Study of gamma irradiation effect on commercial TiO2 photocatalyst. Applied Radiation and Isotopes. 2014; 89: 25–29. https://doi.org/10.1016/j.apradiso.2014.02.001.

[23] Samet L, March K, Brun N, Hosni F, Stephan O, Chtourou R. Effect of gamma radiation on the photocatalytic properties of Cu-doped TiO_2 nanoparticles. Materials Research Bulletin. 2018; 107: 1–7. https://doi.org/10.1016/j.materresbull.2018.07.004.

[24] Zhang Q, Jiang ZW, Wang MZ, Ge XW. Gamma-ray irradiation effects on Bi_2WO_6 photocatalysts. Chinese Journal of Chemical Physics. 2018; 31: 701–706. https://doi.org/10.1063/1674-0068/31/cjcp1805094.

[25] Bourezgui A, Kacem I, Daoudi M, Al-Hossainy AF. Influence of gamma irradiation on the structural, optical, and photocatalytic properties of TiO_2 nanoparticles under controlled atmospheres. Journal of Electronic Materials. 2020; 49: 1904–1921. https://doi.org/10.1007/s11664-019-07887-z.

[26] Jeya P, Keerthana SP, Kungumadevi L, Yuvakkumar R, Ravi G, Kandasami A, *et al*. Gamma irradiation effect on photocatalytic properties of Cu and Sr ions codoped PbS. Environmental Research. 2023; 226: 115651. https://doi.org/10.1016/j.envres.2023.115651.

[27] Bisht R, Joshi GC, Singh JP, Joshi CS. Investigation of the effect of gamma-ray irradiation on SnO2 nanoparticles for photocatalysis application. Nuclear Instruments and Methods in Physics Research Section B: Beam Interactions with Materials and Atoms. 2025; 568: 165862. https://doi.org/10.1016/j.nimb.2025.165862.

[28] Katubi KM, Alsafari IA, Shaheen B, Boukhris I, Al Buriahi MS, Shakir I, *et al*. Gamma irradiated Co_3O_4 for outstanding photocatalytic activity toward removal of pharmaceutical contaminants present in wastewater. Journal of the Korean Physical Society. 2026; 88: 72–86. https://doi.org/10.1007/s40042-025-01487-3.

[29] Wang H, Yuan X, Wu Y, Zeng G, Dong H, Chen X, *et al*. In situ synthesis of In_2S_3/g-C_3N_4 composite with enhanced visible-light photocatalytic activity for organic pollutants. Applied Catalysis B: Environmental. 2015; 174: 445–454. https://doi.org/10.1016/j.apcatb.2015.03.012.

[30] Nefzi C, Yahmadi B, El Guesmi N, Kamoun-Turki N, Ahmed SA. A successful exploitation of gamma-radiation on chalcogenide Cu2InSnS4 towards clean water under photocatalysis approach. Journal of Molecular Structure. 2022; 1251: 131943. https://doi.org/10.1016/j.molstruc.2021.131943.

[31] Al-Kahtani AA, Abou Taleb MF. Photocatalytic degradation of Maxilon C.I. basic dye using CS/CoFe2O4/GONCs as a heterogeneous photo-Fenton catalyst prepared by gamma irradiation. Journal of Hazardous Materials. 2016; 309: 10–19. https://doi.org/10.1016/j.jhazmat.2016.01.071.

[32] Xu J, Zhang L, Shi R, Zhu Y. Chemical exfoliation of graphitic carbon nitride for efficient heterogeneous photocatalysis. Journal of Materials Chemistry A. 2013; 1: 14766–14772. https://doi.org/10.1039/C3TA13188B.

[33] El-Sayed ESR, Abdelhakim HK, Ahmed AS. Solid-state fermentation for enhanced production of selenium nanoparticles by gamma-irradiated Monascus purpureus and their biological evaluation and photocatalytic activities. Bioprocess and Biosystems Engineering. 2020; 43: 797–809. https://doi.org/10.1007/s00449-019-02275-7.

[34] Di Valentin C, Pacchioni G, Selloni A. Origin of the different photoactivity of N-doped anatase and rutile TiO_2. Physical Review B. 2004; 70: 085116. https://doi.org/10.1103/PhysRevB.70.085116.

[35] Gupta B, Melvin AA, Matthews T, Dhara S, Dash S, Tyagi AK. Facile gamma radiolytic methodology for TiO2-rGO synthesis: Effect on photo-catalytic H2 evolution. International Journal of Hydrogen Energy. 2015; 40: 5815–5823. https://doi.org/10.1016/j.ijhydene.2015.02.102.

[36] Bissenova M, Idrissov N, Kuspanov Z, Umirzakov A, Daulbayev C. Hybrid adsorption–photocatalysis composites: a sustainable route for efficient water purification. Materials for Renewable and Sustainable Energy. 2025; 14: 44. https://doi.org/10.1007/s40243-025-00319-5.

[37] Budimir M, Marković Z, Jovanović D, Vujisić M, Mičušík M, Danko M, *et al*. Gamma ray assisted modification of carbon quantum dot/polyurethane nanocomposites: structural, mechanical and photocatalytic study. RSC Advances. 2019; 9: 6278–6286. https://doi.org/10.1039/c9ra00500e.

[38] Saleh MR, El-Gendy RA, Bakier YM, El-Bery HM. Modulating g-C3N4 photocatalyst for H2 production via water splitting: The impact of Schiff base incorporation. Journal of Environmental Chemical Engineering. 2024; 12: 113866. https://doi.org/10.1016/j.jece.2024.113866.

[39] Alhindawy IG, Mahmoud KA. Engineered zirconia nanomaterials for circular environmental and nuclear applications: dual-function design for photocatalytic pollutant degradation and gamma-ray shielding. Advanced Composites and Hybrid Materials. 2025; 8: 317. https://doi.org/10.1007/s42114-025-01379-x.

[40] Fang Z, Zhou Y, Yang Z, Yang C, Zhang J, Hou Y. V2O5-assisted thermal oxidation strategy for synthesizing porous carbon nitride with enhanced photocatalytic NO removal performance. Surfaces and Interfaces. 2025; 60: 106023. https://doi.org/10.1016/j.surfin.2025.106023.

[41] González-Vázquez MY, Carrillo-Martínez CJ, Pinedo-Escobar JA, Escalante-García IL, Martínez AS, González-Rodríguez LM, *et al*. Photocatalytic Degradation of Methyl Orange and Metoprolol by Novel Ternary Photocatalyst TiO2-ZnO/g-C3N4 under UV and Visible Light. 2024. https://doi.org/10.20944/preprints202410.2481.v1. (preprint)